

Monte Carlo simulations of Raman scattered O VI emission lines in symbiotic stars

H. M. Schmid

Institute of Astronomy, ETH-Zentrum, CH-8092 Zürich, Switzerland

Received July 11, accepted October 5, 1991

Abstract. Symbiotic binaries consist of a cool giant and a hot radiation source, which is ionizing a nebula. Recently two emission lines at $\lambda 6825$ and $\lambda 7082$, which are only observed in these systems, have been identified as Raman scattering of O VI $\lambda 1032$ and $\lambda 1038$ photons by neutral hydrogen. Strong O VI lines are produced in the compact H II region, probably near the ionizing component. The conversion into $\lambda 6825$, 7082 photons will occur in the extended atmosphere of the cool giant. Because the scattering geometry in symbiotic stars rotates due to the binary motion, systematic changes in the intensity and polarization of the Raman scattered lines are expected.

In this paper Monte Carlo simulations are presented in order to investigate the flux and polarization properties of the Raman scattered emission lines. Photon paths are calculated for an illuminated atmosphere with scatterings according to the Rayleigh phase matrix and for various scattering and absorption coefficients. Calculated flux and polarization phase curves for symbiotic binaries are given, and diagnostic possibilities of the Raman scattered emission lines explored. The results show that the $\lambda 6825$, 7082 emission lines allow a determination of orbital parameters, such as period, inclination and orientation of the orbital plane. Additionally, information on the geometric structure of the nebular O VI region and on absorbing particles in the outer atmosphere of the red giant can be obtained.

Key words: Raman scattering – symbiotic stars – emission lines – polarization – Monte Carlo simulations

1. Introduction

In about 50 per cent of symbiotic stars strong, broad emission lines are observed at $\lambda 6825$ and $\lambda 7082$. These emission lines have been identified as due to Raman scattering of the O VI resonance lines $\lambda 1032$ and $\lambda 1038$ by neutral hydrogen (Schmid 1989). In this process the incident O VI photon with frequency ν_i excites atomic hydrogen from its ground state $1s^2S$ to an intermediate state from where the Raman scattered photon ν_f is emitted, leaving the atom in the state $2s^2S$. The frequency of the scattered photon is given by the principle of energy conservation $\nu_f = \nu_i - \nu_{if}$, where ν_{if} is the frequency corresponding to the energy difference between initial and final states of atomic hydrogen, $1s^2S$ and $2s^2S$ respectively. Rayleigh scattering differs from Raman scattering due to the fact, that the emitted photon has the same energy as the incoming photon and hydrogen is left

in its ground state. Rayleigh and Raman scattering are dipole type scattering processes which produce large light polarization. Recent spectropolarimetric observations confirmed the presence of polarization in the Raman scattered lines (Schmid & Schild 1990).

The cross section for Raman scattering of O VI photons by neutral hydrogen is small and therefore requires special conditions, if it is to occur in measurable amounts. Up to now the emission lines $\lambda 6825$ and $\lambda 7082$ have only been observed in symbiotic stars. Symbiotic stars are binary systems with orbital periods of several hundred days up to several dozens of years. They show simultaneously spectral features of a cool giant and of an ionized nebula. The usual assumption presents the symbiotic system as consisting of a mass losing red giant and a hot radiation source with $T^* \approx 100\,000\text{K}$, ionizing the nebula within the system. Strong O VI lines are most probably produced in the innermost part of the H II region near the hot, ionizing component and subsequently converted in the extended neutral atmosphere of the cool giant into the $\lambda 6825$, 7082 photons.

The Raman scattered emission lines $\lambda 6825$, 7082 offer various opportunities for investigating symbiotic systems. Interpretation of the observed lines is straightforward because the scattering process is well defined and simple, and the scattering particles (H^0) as well as the origin of the scattered light (O^{+5} -region) are known. A most important advantage compared with other studies on scattering polarization is that all photons in the Raman lines $\lambda 6825$, 7082 are produced in a scattering process. There is no contamination with thermally produced photons originating in a stellar or a nebular source.

The scattering geometry in symbiotic systems changes periodically relative to the line of sight due to the binary motion. Therefore systematic changes are expected not only in the line strengths but also in the amount and orientation of the polarization in the Raman scattered emission lines. Time sequences will allow a determination of the orbital period, the inclination and orientation of the orbital plane. Knowledge of these parameters are for example important for estimating stellar masses and for the interpretation of systems with bipolar nebular structure.

Scattering polarization which varies systematically with orbital phase is also observed in massive binaries (see e.g. St.-Louis et al. 1987; Bastien 1988 and references therein). Theoretical models have been developed to describe the observed time-dependent polarization modulation and to derive the orbital inclination and other parameters of binary systems. In these models stellar light is scattered in an extended, optically thin envelope (e.g. Brown et al.

1978; Rudy & Kemp 1978; Simmons 1983; Dolan 1984; Brown et al. 1989). Contrary to massive binaries, the scattering processes in symbiotic systems occur in a dense and optically thick region (atmosphere of the red giant) where multiple scatterings are frequent and must be taken into account. From this point of view a similar problem is encountered in planetary atmospheres, where sunlight is diffusely reflected. The simulations presented in this work could in principle be adapted to the outer planets where Raman scattering processes due to molecular hydrogen H_2 can be observed (e.g. Cochran 1981).

In this paper the basic properties of Raman scattered emission lines in symbiotic stars are explored. First the rather few available observational data are summarized. It follows a detailed description of the Monte Carlo code for the simulation of the Raman scattered O VI emission lines in symbiotic stars. Results of these simulations for a plane parallel atmosphere are then compared with existing analytical solutions. Then calculations are performed for a system, where O VI photons, which originate in a removed source, are diffusely reflected by a spherical body. The intensity and polarization of the scattered light is calculated for various model parameters in order to investigate the diagnostic possibilities of the Raman scattered emission lines $\lambda\lambda 6825, 7082$ in symbiotic stars.

2. Observational data

The existing observational material for the Raman scattered O VI lines in symbiotic stars allows no detailed analysis. The available observations define, however, a limiting range for the model parameters. In this section observational data of the Raman scattered lines are discussed which are relevant for estimating the scattering geometry and reducing the parameter space for possible model parameters.

The far UV lines O VI $\lambda\lambda 1032, 1038$ are not easily accessible with present instrumentation. However, their flux can be estimated from the intensity of the O V $\lambda 1371$ recombination line and the nebular temperature derived from lines of highly ionized atoms like Ne V and Fe VII. Under nebular conditions a theoretical line ratio $I(\lambda 1032)/I(\lambda 1038) = 2$ is expected for the O VI lines. But in several symbiotic systems a lower line ratio is observed in the ns – np resonance doublets of C IV, N V, Mg II and Si IV. The same may also apply to the O VI doublet.

Fortunately the Raman scattered O VI lines $\lambda\lambda 6825, 7082$ lie in a spectral region easily observable with the standard instrumentation of earthbound observatories. In Fig. 1 a typical spectrum of a symbiotic star showing the Raman scattered emission lines is plotted. Allen (1980) surveys the occurrence and properties of the Raman scattered emission lines for a large sample of symbiotic binaries. He notes that these lines are observed in more than fifty percent of symbiotic stars. Of course, Raman scattering of O VI photons can only occur in high excitation systems, where O^{+5} ions exist in the nebula. If from the catalogue of Allen (1979) only high excitation symbiotics are selected, then the occurrence of Raman scattered O VI emission amounts to about 70 per cent. Thus it can be concluded, that observable $\lambda\lambda 6825, 7082$ emission is common in symbiotic stars as soon as nebular O VI lines $\lambda\lambda 1032, 1038$ are produced. On the other hand no Raman scattered O VI lines have been reported in any other astronomical object. The production of $\lambda\lambda 6825, 7082$ emission seems to demand interaction between a hot ionized nebula and an extended cool giant. Thus an obvious conception for the formation of these lines is as

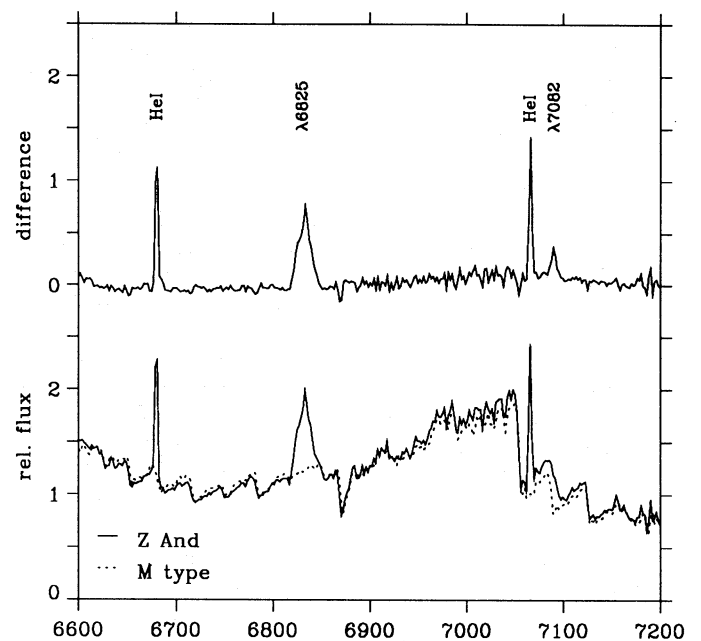


Fig. 1. Raman scattered O VI emission lines in the symbiotic star Z And. The upper spectrum gives the difference between Z And and a M-type spectrum in order to emphasize the emission lines

follows: Strong O VI emission $\lambda\lambda 1032, 1038$ produced in the H II region, most probably near the hot ionizing source, is converted in the extended neutral atmosphere of the cool giant into the $\lambda\lambda 6825, 7082$ photons.

Support for the proposed scattering geometry comes from spectropolarimetric observations made by Schmid & Schild (1990). They found in the symbiotic star He2-38 a polarization of 5.3 and 9.2 per cent in the emission features $\lambda 6825$ and $\lambda 7082$ respectively. Such a large polarization is only expected if a pronounced anisotropy in the scattering geometry is present. This requirement is fulfilled in a binary configuration where photons are produced by or near one component and scattered in the atmosphere of its companion. Only a vanishing net polarization would be measurable if scattering took place mainly in an extended (circumstellar) nebula, because rotational symmetry with respect to the line of sight tends to compensate the polarization from different scattering regions. That the O VI $\lambda\lambda 1032, 1038$ lines are mainly scattered in the atmosphere of the red giant follows also from considerations on scattering opacities. Due to the small Raman scattering cross section large H^0 column densities are needed for the production of $\lambda\lambda 6825, 7082$ lines. Such densities are above all expected in or near the atmosphere of the cool giant (see Schmid 1989). This is confirmed by far UV observations of eclipses in symbiotic stars. In several systems strong wavelength dependent attenuation around $\lambda 1300$ of the continuum radiation from the hot component can be recognized near occultation. Islik et al. (1989) explain this behaviour as being due to Rayleigh scattering by atomic hydrogen. The Rayleigh scattering cross section depends on wavelength, and increases strongly towards the Ly α $\lambda 1215$ resonance transition, with a corresponding heavy effect on the continuum shape. Detailed analysis of the observed spectral changes can be found in Vogel (1991) and Gonzalez-Riestra et al. (1990). This Rayleigh effect is restricted to phases near eclipse, when the radiation of the hot component passes through the extended atmosphere of the cool giant. From atomic

physics it follows that Raman scattering occurs only together with Rayleigh scattering. If a perturbing photon excites hydrogen into a state which can decay incoherently (Raman scattering) also coherent decays (Rayleigh scattering) take place. Therefore the observed eclipse behaviour supports the hypothesis that O VI $\lambda\lambda 1032, 1038$ photons are converted to $\lambda\lambda 6825, 7082$ photons predominately in the vicinity of the red giant.

Another important observational constraint on model parameters comes from the relative strength between the $\lambda 6825$ and $\lambda 7082$ emission. Allen (1980) derived for a statistically significant sample the equivalent widths correlation $EW(\lambda 6825) = 5.5 \pm 0.6 \cdot EW(\lambda 7082)$. According to Fig. 3 in Allen (1980) the observed EW-ratios $\lambda 6825/\lambda 7082$ lie all in the range 3 to 10. The equivalent widths depend slightly on the underlying continuum of the red star, such that the absolute line intensities behave approximately like $I(\lambda 6825) \approx 4 \cdot I(\lambda 7082)$ (Allen 1980). If for the original O VI lines a line ratio $I(\lambda 1032)/I(\lambda 1038) = 2$ is assumed, then the Raman scattering efficiency for the $\lambda 1038$ line is smaller by about a factor two relative to the $\lambda 1032$ line. It follows that either relatively more O VI $\lambda 1038$ photons must be destroyed or escape before Raman scattering takes place or/and that relatively more $\lambda 7082$ photons are destroyed. The absorption and scattering cross sections used in the model calculations should be able to reproduce this behaviour. Interesting in this context are also the spectropolarimetric observations of He II-38, where a larger polarization for the $\lambda 7082$ emission (9.2%) was found compared with the $\lambda 6825$ emission (5.2%). Of course this unique measurement does not define the general behaviour of the Raman scattered emission lines. But the model calculations should show that such a polarization pattern is possible.

3. Model parameters

Our geometric model is a binary system, where an O VI line radiation source illuminates the atmosphere of a spherical body. In this system the O VI photons $\lambda\lambda 1032, 1038$ are produced near the ionizing component S and penetrate at a surface point P into the atmosphere of the cool companion (see Fig. 2). There the photon may undergo different processes: Rayleigh scattering, Raman scattering and absorption. After one or several scatterings the photons may escape from the atmosphere and be observed. The escaping photons have a wavelength of $\lambda 6825$ or $\lambda 7082$ if a Raman scattering process took place. If only Rayleigh scatterings occurred then the wavelength of a reflected photon remains unchanged.

In the calculations we use only models which are rotationally symmetric with respect to the binary axis OS in order to reduce the computational effort.

Photon sources will be described by points at the distance D or a photon beam parallel to the binary axis ($D = \infty$). Extended sources are constructed by rotationally symmetric superpositions of point sources around S . The O VI line radiation originating in the H II region is assumed to be unpolarized. In all models the photon source remains fixed in the frame rotating synchronously with the binary axis (corotation).

The illuminated atmosphere is approximated at each surface point P by a plane parallel, homogeneous and semi-infinite slab. There a polar coordinate system is set up, characterized by the polar axis z perpendicular to the stellar surface, the polar angle ϑ and the azimuthal angle φ . The angles ϑ_0 and φ_0 describe the direction of the incoming photon. The zero point for φ is chosen

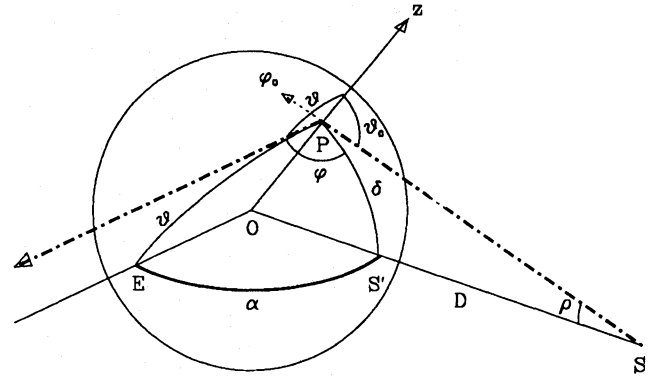


Fig. 2. Scattering geometry. The dashed-dotted line is the trajectory of a reflected photon

such that $\varphi_0 = 180^\circ$. The direction of the escaping photon is given by ϑ and φ in the plane parallel coordinate system or by the direction OE in the binary system.

If we consider only the reflected light from the entire stellar sphere then the problem is rotationally symmetric with respect to the binary axis. The intensity and polarization of the scattered radiation depends only on the angle α between binary axis OS and escape direction OE . We define hereafter the plane defined by OE and OS as principle plane. $\alpha = 0$ means that the photon source is in front of the illuminated star.

For an observer the orientation of the binary system changes periodically due to the orbital motion. The intensity and polarization of the reflected radiation varies therefore with time, depending on the angle α and the orientation of the binary axis with respect to the celestial sphere.

3.1. Description of the line radiation

For the description of intensity and polarization of the Raman scattered emission lines $\lambda\lambda 6825, 7082$ and the diffusely reflected O VI lines $\lambda\lambda 1032, 1038$ the Stokes vector $\mathbf{I} = (I, Q, U, V)$ is employed. The components Q and U are given through $Q = I_0 - I_{90}$, $U = I_{45} - I_{-45}$, where the indices stand for the polarization direction.

In this paper we only study linearly polarized radiation. We can therefore omit the Stokes parameter V for circular polarization, because the radiative transfer equations for I , Q and U do not depend on V .

In the Monte Carlo calculations the resulting Stokes vector \mathbf{I} is obtained by summation of a finite number of photons. Each photon i is described by the Stokes vector $\mathbf{I}_i = (I, \cos 2\gamma_i, \sin 2\gamma_i)$, where the polarization direction of the photon γ_i lies in the interval $[-90^\circ, 90^\circ]$. As can be seen from the Stokes vector \mathbf{I}_i the polarization characteristics of one photon is fully described by the angle γ . We thus need as result of each photon trajectory the escape direction and the polarization angle with respect to a fixed coordinate system.

For the resulting line radiation the Stokes parameters of the collected photons $i = 1 \dots n$ must be summed up according to:

$$I = \sum_i I_i = n, \quad Q = \sum_i \cos 2\gamma_i, \quad U = \sum_i \sin 2\gamma_i. \quad (1)$$

We usually work with the normalized Stokes parameters $p_Q = Q/I$ and $p_U = U/I$ which are defined on the interval $[-1, 1]$. The relative polarization of the reflected radiation is

$$P = \frac{\sqrt{Q^2 + U^2}}{I} \cdot 100\% \quad (2)$$

where P will be expressed in per cent. The polarization angle γ is related to the Stokes parameters through $\tan 2\gamma = U/Q$. Thus γ can be expressed by an arctan-function, where the appropriate quadrant must be considered:

$$\gamma = \frac{1}{2} \arctan\left(\frac{U}{Q}\right) + \bar{\gamma}, \quad \bar{\gamma} = \begin{cases} 0^\circ & Q > 0 \\ +90^\circ & Q < 0, U > 0 \\ -90^\circ & Q < 0, U < 0. \end{cases} \quad (3)$$

3.2. Atomic processes

Three atomic processes are taken into account for the far UV $\lambda\lambda 1032, 1038$ photons: Rayleigh scattering and Raman scattering by atomic hydrogen and continuum absorption. For the red Raman scattered photons $\lambda\lambda 6825, 7082$ only continuum absorption is taken into account. The absorption cross sections can be expressed per hydrogen atom because only homogeneous model atmospheres are considered.

The total Rayleigh and Raman scattering cross sections for neutral hydrogen depend on wavelength. For the individual O VI lines the wavelength dependency of the cross sections are neglected. Only the “mean” values for each O VI line, as given in Schmid (1989), are taken:

$$\begin{aligned} \sigma_{\text{Ram}}(\lambda 1032) &= 6.6\sigma_e, & \sigma_{\text{Ray}}(\lambda 1032) &= 34\sigma_e, \\ \sigma_{\text{Ram}}(\lambda 1038) &= 2.0\sigma_e, & \sigma_{\text{Ray}}(\lambda 1038) &= 6.7\sigma_e. \end{aligned} \quad (4)$$

where $\sigma_e = 6.65 \cdot 10^{-25} \text{ cm}^2$ is the Thomson cross section.

In each Rayleigh and Raman scattering process the direction and polarization of the scattered photon is evaluated according to the pure Rayleigh phase matrix \mathbf{R} based on the assumption that the scattering particles are randomly orientated. We disregard in the calculations the influence of depolarizing collisions. If the intensity and polarization of the incident radiation beam onto a scattering particle is described by the Stokes vector \mathbf{I}_s then the scattered radiation \mathbf{I}'_s is obtained from the equation

$$\mathbf{I}'_s(\theta_s, \phi_s) = \frac{\sigma}{4\pi} \mathbf{R} \mathbf{I}_s. \quad (5)$$

θ_s and ϕ_s are the polar and azimuthal scattering angle respectively. If the Stokes vectors \mathbf{I}_s and \mathbf{I}'_s refer to the plane of scattering, then the phase matrix has the form (see e.g. Stenflo 1976):

$$\mathbf{R} = \frac{3}{4} \begin{pmatrix} \cos^2 \theta_s + 1 & \cos^2 \theta_s - 1 & 0 \\ \cos^2 \theta_s - 1 & \cos^2 \theta_s + 1 & 0 \\ 0 & 0 & 2 \cos \theta_s \end{pmatrix}. \quad (6)$$

In the Monte Carlo calculations the orientation of the scattering plane is not known in advance, but evaluated from a random number. We use therefore the local azimuthal scattering angle ϕ_s for the orientation of the scattering plane relative to the polarization direction of the incoming photon. Thus in this local coordinate system the polarization direction of the incoming photon is by definition $\gamma = -\phi_s$ and the corresponding Stokes vector $\mathbf{I}_s = (1, \cos 2\phi_s, -\sin 2\phi_s)$.

The continuum absorption cross section for the far UV radiation κ_{uv} is not well known for cool giants atmospheres. Most likely κ_{uv} is dominated by the photoionization cross section of C⁰ and other neutral atoms. In symbiotic binaries the radiation from the hot component may change the ionization structure. In all calculations the absorption cross section κ_{uv} for $\lambda 1032$ and $\lambda 1038$ are taken as equal.

For the red Raman scattered photons $\lambda 6825$ and $\lambda 7082$ only absorption processes are taken into account because in this wavelength domain coherent scattering can be ignored. Thus after a Raman scattering process only photons which are flying upwards in the atmosphere have a non-zero probability to escape. All red Raman photons penetrating further into the atmosphere are destroyed. For the M-type giants in symbiotics, the pronounced wavelength dependence of the opacities due to the TiO molecule may be important. The weaker emission at $\lambda 7082$ coincides roughly with a strong TiO band head at $\lambda 7054$ as can be seen in Fig. 1. We explore therefore also the effect of individual absorption cross sections $\kappa(\lambda 6825) \neq \kappa(\lambda 7082)$ on the Raman scattered lines.

3.3. Geometric transformations

Three different coordinate systems are used in our calculations for the description of the photon trajectories and a fourth, the celestial coordinates, are needed for comparison with observations. There follow some comments on the geometric transformations between the different coordinate systems.

3.3.1. Scattering plane – plane parallel system

Each scattering process is described first in a local system defined by the scattering plane and the polarization direction of the incoming photon. The direction changes are defined in this system by the polar θ_s and azimuthal ϕ_s scattering angles. They are evaluated from random numbers. The polarization change $\Delta\gamma_s(\theta_s, \phi_s)$ is given by the scattering angles (see Eqs. (23) and (28)).

These direction and polarization changes must be transformed into the polar coordinate system for the plane parallel atmosphere ($\vartheta, \varphi, \gamma_p$). In this system the polarization direction γ_p is measured with respect to the meridional planes going through the polar axis z . The scattering plane is defined by the propagation directions of the incoming and scattered photon given in Fig. 3 by A_1 and A_2 or by $(\vartheta_1, \varphi_1, \gamma_1)$ and $(\vartheta_2, \varphi_2, \gamma_2)$. The direction and polarization angles for the scattered photon ϑ_2, φ_2 and γ_2 are obtained from $\varphi_1, \vartheta_1, \gamma_1$ and $\theta_s, \phi_s, \Delta\gamma_s$ using trigonometric relations.

After a scattering process the photon may escape. If the plane parallel problem is treated, the photon is registered in the appropriate bin for the escape direction ϑ and φ and the polarization direction γ_p is transformed into the Stokes parameters $Q = \cos 2\gamma_p$ and $U = \sin 2\gamma_p$. Thus we use the convention $Q = 1$ for photons which are polarized parallel to a meridional plane. For the plane defined by $\varphi = 0^\circ, 180^\circ$ (scattering plane perpendicular to the surface) the polarization in the U -direction vanishes due to the symmetry of the scattering problem with respect to this plane. Thus the radiation is polarized either parallel $Q > 0$ or perpendicular $Q < 0$.

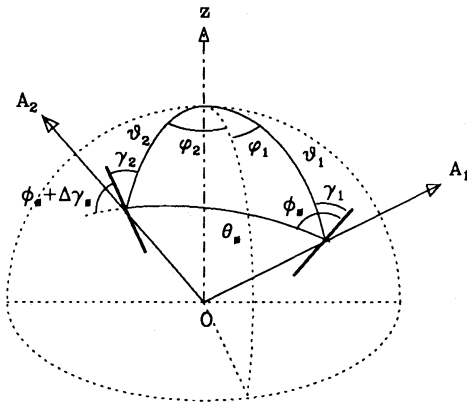


Fig. 3. Propagation and polarization direction of the incoming and the scattered photon in the local (relative to the scattering plane) and the plane parallel coordinate system

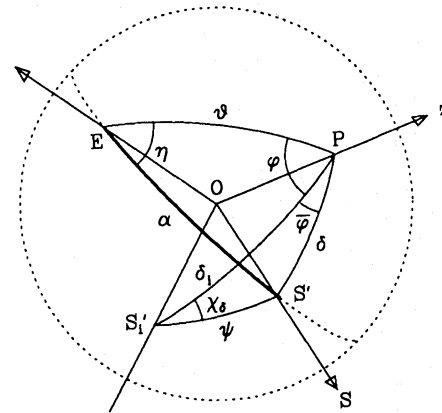


Fig. 4. Spherical triangles for transformations between the double star and the plane parallel coordinate system

3.3.2. Plane parallel system – binary system

If we are interested in the emerging radiation from the whole illuminated star then the photon parameters must be transformed between the plane parallel system and the binary coordinate system. The photon parameters are first given in the binary system through the properties of the photon source. Then the photon scattering path is treated in the plane parallel system ($\vartheta, \varphi, \gamma_p$). Escaping photons are again described in the binary system (α, γ). Due to rotational symmetry the description of the escape direction can be reduced to the angle α between binary axis and line of sight.

We assume first that a photon is released from a point S located on the axis of symmetry (see Fig. 2). The photon is described in the binary system by the distance D of the source S and the direction of the photon ϱ . From ϱ and D follow δ and the angle of incidence ϑ_0 for the plane parallel atmosphere model. The coordinate system at P is orientated such that $\varphi_0 = 180^\circ$. The polarization direction of the incoming photon γ_0 can be chosen randomly, because the photon source emits unpolarized light. The direction and polarization of the escaping photon is given by the angles ϑ , φ and γ_p as calculated from the photon path in the plane parallel atmosphere model. The polar angle α of the escape direction is obtained from δ , ϑ and φ using trigonometric relations for the spherical triangle S', E, P .

If we consider extended photon sources, which are composed of an ensemble of single points S_i , then a released photon is additionally characterized by the separation ψ of S_i or S'_i from the binary axis and an azimuthal angle χ_δ for the photon direction (see Fig. 4). Because we presupposed rotationally symmetric sources no azimuthal angle is needed for describing the position of S'_i . The angles δ_i and ϑ_0 are again given by ϱ and D . Using trigonometric relations for the triangles drawn in Fig. 4 the quantities δ and $\bar{\varphi}$ are derived from δ_i , ψ and χ_δ and finally the polar angle α from δ , ϑ and $\varphi + \bar{\varphi}$.

The polarization direction in the plane parallel system γ_p is measured relative to the meridional plane given by the propagation direction and the axis z . For an escaping photon this plane is defined in the binary system by the points O , P and E and has the inclination η with respect to the principle plane. Thus the direction of the photon polarization relative to the principle plane is obtained by the transformation $\gamma = \gamma_p \pm \eta$. If the plus or the minus sign must be used depends on the sign of the angle

φ what is equivalent with reflection from the “upper” or the “lower” hemisphere (with respect to the principle plane).

The reflected radiation is finally described by the Stokes vector $I(\alpha)$. In the coordinate system (α, γ) we use the Stokes parameter $Q = 1$ for photons which are polarized parallel to the principle plane. The U component is expected to vanish, because scattering geometry is symmetric with respect to the principle plane, so that the polarization in the 45° and -45° -directions compensate each other. Thus we can fully describe the intensity and polarization by the two Stokes components $I(\alpha)$ and $Q(\alpha)$.

3.3.3. Binary system – observer’s system

A further transformation is needed to compare the calculations with observations. The intensity and polarization, which change periodically with the orbital angle ω , depend on the inclination i of the orbital plane. Further the position angle of the ascending node Ω relative to north must be known to map the polarization direction γ_c with respect to the celestial sphere. We consider only systems with circular orbits. This is a reasonable approximation as radial velocity measurements for symbiotic stars revealed no or only small eccentricities (Garcia & Kenyon 1988).

The observable quantities are described in the celestial coordinate system with the Stokes vector I_c with the parameters I_c , $Q_c = I_N - I_E$ and $U_c = I_{NE} - I_{NW}$ or with the normalized Stokes parameters $p_Q = Q_c/I_c$ and $p_U = U_c/I_c$. Q_c and U_c are positive for polarization directions north and north-east respectively. The intensity and polarization light curves $I_c(\omega, i, \Omega) = (I_c(\omega, i), Q_c(\omega, i, \Omega), U_c(\omega, i, \Omega))$ can be constructed from the Stokes vector $I(\alpha) = (I(\alpha), Q(\alpha), 0)$ for the reflected radiation given in the coordinates of the binary system.

Due to the motion the points O and S on the binary axis describe in the celestial system ellipses for which the eccentricity increases with the orbital inclination. The mayor axis of these ellipses coincides with the line of node, what is also equal to the quadrature phases or the phases of maximum elongation ($\alpha = 90^\circ$). On the minor axis lie the conjunction phases when either the largest or the smallest fraction of the illuminated hemisphere is visible. We set $\omega = 0^\circ$ for the phase when the maximum fraction of the illuminated hemisphere is visible. Thus the orientation of the ascending node Ω coincides with the binary axis for phase $\omega = 270^\circ$.

The intensity of the reflected radiation depends on the apparent distance D' between the points O and S (apparent length of binary axis). D' is given in the two systems by $D' = D \sin \alpha$ and $D' = D (\cos^2 \omega \cos^2 i + \sin^2 \omega)^{1/2}$. For a conversion $\omega \rightarrow \alpha$ we must additionally consider the corresponding quadrant as follows:

$$\begin{aligned} \alpha_{\omega,i} &= \arcsin \left(\sqrt{\cos^2 \omega \cos^2 i + \sin^2 \omega} \right), & 0^\circ \leq \omega \leq 90^\circ, \\ & & 270^\circ \leq \omega \leq 360^\circ; \\ \alpha_{\omega,i} &= 180^\circ \\ & - \arcsin \left(\sqrt{\cos^2 \omega \cos^2 i + \sin^2 \omega} \right), & 90^\circ \leq \omega \leq 270^\circ. \end{aligned} \quad (7)$$

The apparent direction of the binary axis with respect to the celestial north pole is

$$\varpi_c = \pm \left[\arctan \left(\frac{\tan \omega}{\cos i} \right) + 90^\circ \right] + \Omega. \quad (8)$$

The plus sign stands for counterclockwise and the minus sign for clockwise rotation.

The Stokes parameters relative to the celestial coordinates are thus given by

$$\begin{aligned} I_c(\omega, i) &= I(\alpha_{\omega,i}), \\ Q_c(\omega, i, \Omega) &= Q(\alpha_{\omega,i}) \cdot \cos 2\varpi_c, \\ U_c(\omega, i, \Omega) &= Q(\alpha_{\omega,i}) \cdot \sin 2\varpi_c. \end{aligned} \quad (9)$$

Using Eq. (3) for Q_c and U_c gives the polarization direction γ_c in the celestial system. In almost all cases the reflected radiation is polarized perpendicular to the binary axis $Q(\alpha_{\omega,i}) < 0$, so that $\gamma_c = \varpi_c \pm 90^\circ$.

4. The Monte Carlo technique

This section describes how the Monte Carlo method is applied to compute the formation of Raman scattered O VI lines. A guideline for the Monte Carlo method for random walk problems is given in Cashwell & Everett (1959). Basically the history of many photons are followed from the source until they escape from the scattering region or are destroyed by an absorption process. After a sufficiently large number have escaped, the reflected intensity and polarization of the Rayleigh scattered O VI lines $\lambda\lambda 1032, 1038$ and the red Raman scattered $\lambda\lambda 6825, 7082$ lines can be established. The quantities describing one full photon trajectory are calculated according to the following scheme.

O VI photons:

- (1) direction and polarization for the released photon from the source
- (2) free path length until photon undergoes interaction
- (3) escape from the scattering region is examined
 - (a) escape: direction and polarization of O VI photon is stored
 - (b) no escape: go to (4)
- (4) coordinates of the collision
- (5) type of collision
 - (a) Rayleigh scattering: go to (6)
 - (b) Raman scattering: go to (7)
 - (c) absorption: end
- (6) new direction and polarization, go to (2)

Raman scattered photons:

- (7) new direction and polarization

- (8) free path length until photon undergoes interaction

- (9) escape from scattering region is examined

- (a) escape: direction and polarization of Raman scattered photon is stored
- (b) absorption: end

4.1. Probability distribution functions

In the Monte Carlo technique the quantities describing the photon trajectories, like path length, scattering angles or type of collision are characterized by probability density functions $\rho(x)$ (see Cashwell & Everett 1959). $\rho(x)$ is normalized in an interval $[a, b]$ such that

$$\int_a^b \rho(\xi) d\xi = 1. \quad (10)$$

A random event for the process described by $\rho(x)$ is simulated by choosing a random number r from an uniform distribution $0 \leq r < 1$, so that

$$r = \mathcal{P}(x) = \int_a^x \rho(\xi) d\xi. \quad (11)$$

$\mathcal{P}(x)$ is called the probability distribution function and the random event x must be evaluated solving the inverse equation

$$x = \mathcal{P}^{-1}(r). \quad (12)$$

Often no simple analytical expression for the inverse function $\mathcal{P}^{-1}(r)$ can be found, so that quite time consuming procedures are needed for the evaluation of x . A powerful alternative is the *rejection method*, especially when $\rho(x)$ is easily computable (see Cashwell & Everett 1959). The method requires neither the indefinite integral $\mathcal{P}(x)$, nor its inverse function. The rejection method consists of choosing random points (ξ, η) in a rectangle, which contains the distribution function $\rho(x)$. The rectangle is defined by $a \leq \xi \leq b$ and $0 \leq \eta \leq c$. The upper boundary c must fulfill the condition $c \geq \rho(\xi)$ for all ξ . The random points are uniformly distributed in the rectangle. If all points lying above the probability density function $\eta > \rho(\xi)$ are rejected, then the remaining points are uniformly distributed on the area below the curve $\rho(x)$. They form a probabilistic description of the process defined by $\rho(x)$. The rectangle can also be replaced by a comparison function $f(x)$, where $f(x) \geq \rho(x)$ for all x . In order to obtain a uniform distribution of points on the area below the function $f(x)$, the values ξ must be evaluated from the function $f(x)$ by the inversion method described above. The second coordinate η lies then for a given ξ in the interval $0 \leq \eta \leq f(\xi)$. Again points (ξ, η) are rejected if $\eta > \rho(\xi)$. Using a comparison function can be convenient to enhance the efficiency of the rejection method.

4.1.1. Photon source

A photon released from a source (at a given distance D) is defined by its propagation and polarization directions. For point sources S located on the binary axis the photon is sufficiently described by the polar direction angle ϱ and the polarization angle γ . For extended sources we need additionally the angles ψ and χ_δ (see Fig. 4) to characterize the origin S_i of the photon and its direction. There follow probabilistic expressions for all these quantities.

Polarization angle. We assume zero polarization for the O VI lines originating from the source near the hot component. This means that the polarization directions γ of the O VI photons is equidistributed on the interval $[-\pi/2, \pi/2]$. The probability density function is $\rho(\gamma) = 1/\pi$ and the corresponding distribution function

$$\mathcal{P}(\gamma) = \frac{1}{\pi} \int_{-\pi/2}^{\gamma} d\gamma = \frac{1}{\pi} \left(\gamma + \frac{\pi}{2} \right) = r. \quad (13)$$

Thus the polarization direction γ for an initial photon follows from the random number r and the equation $\gamma = \mathcal{P}^{-1}(r)$ or

$$\gamma = \pi \left(r - \frac{1}{2} \right). \quad (14)$$

Polar direction angle. For an isotropic photon source the emitted flux as function of the polar angle ϱ behaves like $F(\varrho) d\varrho = (F_S/2) \sin \varrho d\varrho$, where F_S is the total source luminosity. This distribution must be normalized such that the fraction of photons which illuminate the reflecting star is equal to 1. This fraction f_ϱ is defined by the tangent cone from point S (or S_i) to the spherical star. Its boundary is given by $\varrho_{\max} = \arcsin(R/D)$ and the normalization factor has the form

$$f_\varrho = \int_0^{\varrho_{\max}} \frac{1}{2} \sin \varrho d\varrho = \frac{1}{2} (1 - \cos \varrho_{\max}). \quad (15)$$

The probability distribution for the direction angle is given by

$$\mathcal{P}(\varrho) = \frac{1}{f_\varrho} \int_0^{\varrho} \frac{1}{2} \sin \varrho d\varrho = \frac{1 - \cos \varrho}{1 - \cos \varrho_{\max}} \quad (0 \leq \varrho \leq \varrho_{\max}). \quad (16)$$

The angle ϱ can be evaluated from a random number r using the corresponding inverse function

$$\varrho = \arccos(1 - r + r \cos \varrho_{\max}). \quad (17)$$

Extended sources. We adopt in this work only extended sources which are shaped like a spherical cap with constant surface brightness and boundary ψ_{\max} . In this case the distribution of point sources $S_i(\psi)$ is mathematically analog to the distribution $\mathcal{P}(\varrho)$ for the direction angles of the released photons (Eq. (16)). Thus Eq. (17) for ϱ can be adapted for ψ :

$$\psi = \arccos(1 - r + r \cos \psi_{\max}). \quad (18)$$

The azimuthal photon direction χ_δ is equidistributed on the interval $[-\pi, \pi]$, because each point S_i represents an isotropic photon source. Therefore $\chi_\delta(r)$ follows in analogy to Eqs. (13) and (14)

$$\chi_\delta = 2\pi \left(r - \frac{1}{2} \right). \quad (19)$$

4.1.2. Photon processes

We determine also from random numbers the type and locus of collisional processes and, if scattering occurs, the direction and polarization changes.

Type of collision. The type of collision follows directly from the normalized probability ρ_i for each process considered. Process k takes place if the random number r lies in the interval

$$\sum_{i=1}^{k-1} \rho_i \leq r < \sum_{i=1}^k \rho_i. \quad (20)$$

In our treatment ρ_i corresponds to the cross section of one particular process (e.g. σ_{Ram}) divided by the total cross section κ_{tot} .

Free path length. The probability that a photon undergoes a collision in a column density interval is $\rho(\ell) d\ell = e^{-\ell \kappa_{\text{tot}}} d\ell$. ℓ is the column density from the previous scattering point or from the surface point where the photon penetrates into the atmosphere. The total cross section κ_{tot} is the sum of all absorption and scattering cross sections. Because a homogeneous atmosphere is assumed we can use the optical depth along the photon path $\tau_\ell = \ell \kappa_{\text{tot}}$ as parameter. We thus obtain the probability distribution function

$$\mathcal{P}(\tau_\ell) = \int_0^{\tau_\ell} e^{-\tau} d\tau = 1 - e^{-\tau_\ell} = r. \quad (21)$$

In our plane parallel atmosphere model only the vertical optical depth τ is of interest. The change in the vertical optical depth $\Delta\tau$ from one collision to another is given by $\Delta\tau = -\tau_\ell \cos \vartheta$, where $\cos \vartheta$ is negative and $\Delta\tau$ positive for directions into the atmosphere. Combining this substitution with the probability function given above results in the following relation between random number r and the optical depth change $\Delta\tau$:

$$\Delta\tau = \cos \vartheta \cdot \ln(1 - r). \quad (22)$$

The optical depth of the new collision τ' follows then from τ of the previous collision and the optical depth change according to $\tau' = \tau + \Delta\tau$. The photon has escaped from the atmosphere if τ' is negative.

Scattering angles. For Rayleigh and Raman scattering the differential cross section depends on the polar and azimuthal scattering angles θ_s and ϕ_s respectively. The probability distribution function $\mathcal{P}(\theta_s, \phi_s)$ for the direction change in the scattering process follows from Eq. (5). We recall that the scattering angles and the Stokes vectors refer to the plane of scattering. From Eq. (5), and setting $\sigma = 1$, the individual components of I'_s are obtained:

$$\begin{aligned} I'_s &= \frac{3}{16\pi} (\cos^2 \theta_s + 1 + (\cos^2 \theta_s - 1) \cos 2\phi_s), \\ Q'_s &= \frac{3}{16\pi} (\cos^2 \theta_s - 1 + (\cos^2 \theta_s + 1) \cos 2\phi_s), \\ U'_s &= \frac{3}{16\pi} (2 \cos \theta_s \sin 2\phi_s). \end{aligned} \quad (23)$$

The probability distribution function $\mathcal{P}(\theta_s, \phi_s)$ follows from the integration of the intensity component I'_s over all solid angles:

$$\mathcal{P}(\theta_s, \phi_s) = \int_0^{\theta_s} \int_{-\pi}^{\phi_s} I'_s(\theta, \phi) \sin \theta d\phi d\theta. \quad (24)$$

The scattering angles lie in the intervals $0 \leq \theta_s \leq \pi$ and $-\pi \leq \phi_s \leq \pi$. In order to evaluate the scattering angles from random numbers we decompose the two-dimensional distribution function $\mathcal{P}(\theta_s, \phi_s)$ into the one-dimensional functions $\mathcal{P}(\theta_s)$

and $\mathcal{P}_\theta(\phi_s)$. The first probability distribution function is obtained from Eq. (24) by integration over the angle ϕ :

$$\mathcal{P}(\theta_s) = \int_0^{\theta_s} \frac{3}{8} (\cos^2 \theta + 1) \sin \theta \, d\theta = r. \quad (25)$$

For the derivation of the azimuthal scattering angle the probability density function $\rho_\theta(\phi)$ must be normalized for all possible polar angles θ_s according to:

$$\int_{-\pi}^{+\pi} \rho_\theta(\phi) \, d\phi = 1. \quad (26)$$

This gives the probability distribution function

$$\mathcal{P}_\theta(\phi_s) = \frac{1}{2\pi} \int_{-\pi}^{\phi_s} 1 + \frac{\cos^2 \theta_s - 1}{\cos^2 \theta_s + 1} \cos 2\phi \, d\phi = r. \quad (27)$$

For the evaluation of both scattering angles θ_s and ϕ_s the rejection method is applied.

The polarization direction of the scattered photon γ'_s with respect to the scattering plane ($\gamma_s = -\phi_s$) can be calculated from the Stokes parameters according to

$$\gamma'_s = -\phi_s + \Delta\gamma_s = \frac{1}{2} \arctan\left(\frac{U'_s}{Q'_s}\right) + \bar{\gamma}, \quad (28)$$

where $\bar{\gamma}$ is 0° , $+90^\circ$ or -90° according to the cases in Eq. (3).

4.2. Statistical weights

Weights are powerful means for saving computer time and improving the statistics of Monte Carlo simulations. In the present code such a procedure is employed for the escaping Raman photons. Instead of calculating for the Raman photons with upward direction the random free path length until absorption and check whether the photon can escape or not, only the escape probability w is determined. The escape probability for Raman photons depends on the optical depth τ_{red} and the escape direction $\cos \vartheta$ with respect to the normal:

$$w = e^{-\tau_{\text{red}} / \cos \vartheta}. \quad (29)$$

The optical depth in the red can easily be deduced from the UV-optical depth with the relation

$$\tau_{\text{red}} = \tau_{\text{uv}} \frac{\kappa_{\text{red}}}{\sigma_{\text{Ray}} + \sigma_{\text{Ram}} + \kappa_{\text{uv}}}. \quad (30)$$

Thus all upward flying Raman photons are stored but also weighted with the previously determined value w . The number of absorbed photons is enhanced by the complement $1 - w$. Especially for large absorption cross sections κ_{red} much more photons contribute with this method to the resulting radiation field so that the statistic is significantly improved. Another advantage is that the reflected radiation field can be summed up at the same time for various weights w corresponding to various absorption parameters κ_{red} .

4.3. Statistical errors

In the Monte Carlo simulation the accuracy increases only as the square root of the sampled photons. It is therefore important to estimate the statistical errors of the calculated results. According to the photon or Poisson statistic the error (standard deviation) for the reflected intensity is

$$\sigma_I = \sqrt{N_i} \quad (31)$$

where N_i is the number of collected photons in a particular (direction) bin i .

Results for the calculated polarization will mainly be expressed by the normalized Stokes parameter p (p_Q and p_U). For the description of the statistical error σ_p an analog treatment as for polarization observations is used. It is assumed that the results can be treated as two independent intensity “measurements” I_\parallel , I_\perp (where $I = I_\parallel + I_\perp$) of parallel and perpendicular polarized photons with individual errors $\sqrt{N_\parallel}$ and $\sqrt{N_\perp}$ as above for the total intensity I . σ_p follows from the basic rules for error propagation. The normalized Stokes parameter is defined by

$$p = \frac{I_\parallel - I_\perp}{I_\parallel + I_\perp} \quad (32)$$

and the corresponding variance σ_p^2

$$\sigma_p^2 = \left(\frac{\partial p}{\partial I_\parallel}\right)^2 \sigma_{I_\parallel}^2 + \left(\frac{\partial p}{\partial I_\perp}\right)^2 \sigma_{I_\perp}^2 = \frac{4I_\parallel I_\perp}{I^3}. \quad (33)$$

This result can also be transformed into

$$\sigma_p = \sqrt{\frac{1-p^2}{I}} = \sqrt{\frac{1-p^2}{N_i}}. \quad (34)$$

For calculations with finite absorption cross section κ_{red} , where weighted photon counts are summed up, the same formula for the statistical errors are applied for simplicity. This underestimates the accuracy, because much more (weighted) photons contribute to the resulting photon numbers (N_i). Thus in these cases the statistical errors as indicated by error bars in the figures are somewhat overestimated.

5. General properties of the Raman scattered O VI lines

In this chapter some basic properties of Raman scattered radiation produced in a Rayleigh scattering atmosphere are explored. The results of the Monte Carlo calculations are first discussed for the plane parallel case. Then we describe the general intensity and polarization properties of the Rayleigh and Raman scattered O VI lines reflected from a spherical body.

Plane parallel calculations have the advantage that they can be compared with previous investigations on Rayleigh scattering atmospheres, so that the special properties of the Raman scattering problem are more easily understood. This comparison is also a test for the Monte Carlo simulations. For a review and a general discussion on diffusely reflected radiation from scattering atmospheres see van de Hulst (1980). In the multiple scattering theory the scattering albedo a is used as parameter. It corresponds to the probability that a photon is scattered coherently.

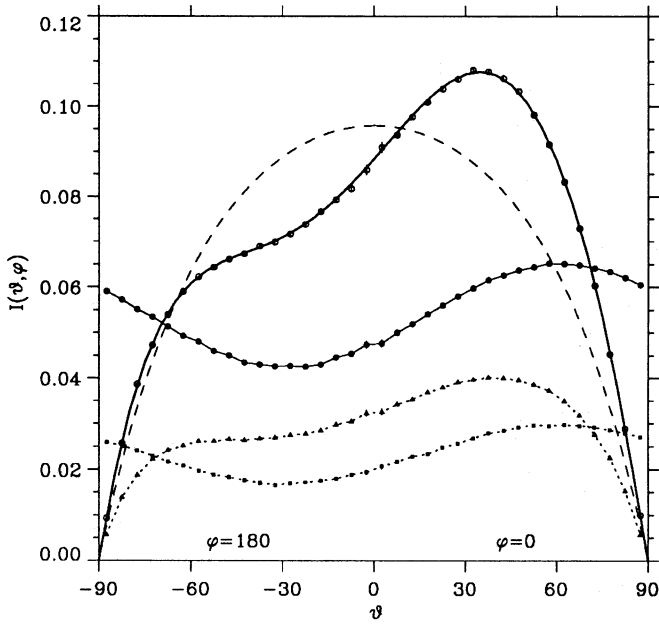


Fig. 5. Rayleigh and Raman scattered radiation reflected from a plane parallel atmosphere into the perpendicular scattering plane ($\vartheta_0 = 60^\circ$). Intensities I_{Ray} (open circles) and I_{Ram} (filled symbols) for zero absorption (circles), $\kappa_{\text{uv}} = 0.4$ (squares) and $\kappa_{\text{red}} = 0.4$ (triangles) with 1σ error bars. The analytical solution for Rayleigh scattering (thick solid line) and isotropic scattering (dashed line) are also shown

The scattering albedo for the O VI photons is defined by the cross sections

$$a = \frac{\sigma_{\text{Ray}}}{\sigma_{\text{Ray}} + \sigma_{\text{Ram}} + \kappa_{\text{uv}}} \quad (35)$$

Throughout this chapter the scaled Rayleigh and Raman scattering cross sections $\sigma_{\text{Ray}} = 0.8$ and $\sigma_{\text{Ram}} = 0.2$ in units of σ_{tot} are used, where $\sigma_{\text{tot}} = \sigma_{\text{Ray}} + \sigma_{\text{Ram}}$ is the total scattering cross section. These values form reasonable approximations for the O VI photon scattering processes by atomic hydrogen (see Eq. (4)). For the absorption cross sections κ_{red} and κ_{uv} values in the range 0.05 – 5.0 (in units of σ_{tot}) are explored.

5.1. Plane parallel atmosphere

We consider a plane parallel atmosphere illuminated by a parallel and unpolarized beam of O VI photons expressed by the radiation flux F_0 or by the number of incoming photons N_0 . The diffusely reflected O VI photons and the Raman scattered photons are then characterized by the Stokes vectors $I_{\text{Ray}}(\vartheta_0, \vartheta, \varphi - \varphi_0)$ and $I_{\text{Ram}}(\vartheta_0, \vartheta, \varphi - \varphi_0)$. In order to limit our discussion, only results for a fixed angle of incidence, $\vartheta_0 = 60^\circ$, and for the perpendicular scattering plane $\varphi - \varphi_0 = 0^\circ$ or 180° are given. For this special scattering plane the polarization in the U-direction vanishes, due to the symmetry in the scattering geometry. We use $I(\vartheta)$ and the normalized Stokes parameter $p_Q(\vartheta) = Q/I$ for the description of the reflected radiation.

In the calculations $N_0 = 10^8$ photons were followed through. The reflected photons are counted in direction bins, defined by the central angles $\vartheta_i = 2.5^\circ + i \cdot 5^\circ$, $i = -18, \dots, +17$ and $\varphi = 0^\circ$ or 180° . The bin widths are $\Delta\vartheta = 5^\circ$, $\Delta\varphi = 10^\circ$. The solid angle covered by one bin Ω_i is thus $\Omega_i = |\sin \vartheta_i| \cdot \pi^2 / (18 \cdot 36)$. In order

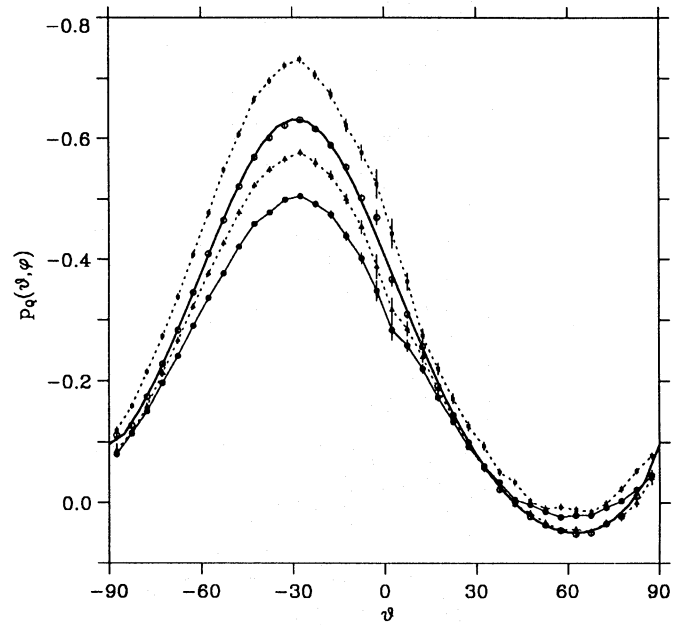


Fig. 6. The same as Fig. 5 for the normalized Stokes parameter $p_Q(\vartheta)$

to obtain the reflected intensity I_i relative to the incoming flux F_0 per unit solid angle and unit surface area, the counts N_i must be scaled according to $I_i = N_i / (\Omega_i N_0)$. However, the statistical errors must still be calculated from the photon counts N_i . The errors are large for angles ϑ_i near zero, where the bin size, and therefore N_i , is small. The count rates lie typically between 10^4 and 10^5 photons for Raman and Rayleigh scattering and go down to $\approx 10^3$ near $\vartheta = 0$. The corresponding statistical errors are thus typically smaller than 1% and can reach about 3% for perpendicular escape directions (see Sect. 4.3).

In Figs. 5 and 6 the calculated intensities and polarizations for the Rayleigh scattered O VI radiation are plotted with open circles and for the Raman scattered O VI radiation $I_{\text{Ram}}(\vartheta)$ with filled symbols.

For the Rayleigh scattered radiation the chosen parameters correspond to the problem of diffuse reflection by a non-conservative Rayleigh scattering atmosphere with scattering albedo $a = 0.8$. The thick solid line is the analytical (exact) solution for this problem calculated from the formulae and tabulations given by Abhyankar & Fymat (1970, 1971). The results of the Monte Carlo calculations agree excellently with the analytical solution. The dashed line is the analytical solution for isotropic scattering ($a = 0.8$) taken from Chandrasekhar (1950). Note that in this work the intensity reflected per unit surface area is plotted, and not per unit area perpendicular to the direction of emergence as in the figures of Abhyankar & Fymat (1970) or Chandrasekhar (1950). The difference amounts to a factor $\cos \vartheta$.

Clearly visible is the difference between the intensity curves for isotropic scattering, Rayleigh scattering and Raman scattering. The Rayleigh curve has a pronounced maximum around $\vartheta \approx 35^\circ$ because Rayleigh scattering prefers forward and backward directions, according to the scattering matrix given in Eq. (6). Although the same scattering matrix applies for Raman scattering, the curve $I_{\text{Ram}}(\vartheta)$ differs strongly from $I_{\text{Ray}}(\vartheta)$. The intensity of the Raman scattered radiation is much higher for grazing emergence, what is equivalent to extreme limb brightening. This is due to the fact, that Rayleigh and Raman scatterings of far

UV photons take place in a region where the atmosphere is still transparent for the red Raman photons. They can therefore also escape for large zenith angles. If an absorption coefficient $\kappa_{\text{red}} \neq 0$ is introduced then grazing emergence is strongly suppressed and the shape of the intensity curve $I_{\text{Ram}}(\vartheta, \kappa_{\text{red}} = 0.4)$ becomes similar to $I_{\text{Ray}}(\vartheta)$. Thus the coefficient κ_{red} changes predominantly the intensity of the Raman scattered radiation for large zenith angles $\vartheta \approx 70^\circ - 90^\circ$. Variations in the absorption coefficient κ_{uv} change the Raman scattered intensity for all scattering angles simultaneously without significant changes in the shape of the intensity curve.

Figure 6 gives the normalized polarization $p_Q(\vartheta) = Q/I$ for the Rayleigh and Raman scattered radiation. Again the analytical solution for the Rayleigh scattering atmosphere is included. All polarization curves in Fig. 6 show the same pattern. Maximum polarization P_{max} occurs for perpendicular scattering angles $\vartheta - \vartheta_0 = 90^\circ$ as expected from the Rayleigh phase matrix. The polarization of the reflected radiation is mainly determined by those photons which undergo only one scattering process. The multiple scattered photons give as a rough approximation an almost unpolarized contribution to the radiation field. Thus multiple scatterings mainly lower the polarization. For backscattering a small negative polarization (parallel to the perpendicular scattering plane) is present. For these directions single scatterings are not or only little polarized, so that the polarization contribution of multiple scattered photons dominates (see e.g. van de Hulst 1980).

Absorption enhances mainly the amount of polarization, while the shape of the polarization curves is less affected. As described in Abhyankar & Fymat (1970) the polarization of Rayleigh scattered radiation increases for increasing continuum absorption, because then the depolarizing effects of multiple scatterings are reduced. The same happens also for the Raman scattered radiation.

5.2. Reflection from a spherical body

The Monte Carlo calculations for a plane parallel atmosphere can also be adapted to an illuminated spherical body. Due to the rotational symmetry only the angle α between binary axis and line of sight remains as geometric parameter. The reemitted radiation will be described by the Stokes vectors $I_{\text{Ray}}(\alpha)$ and $I_{\text{Ram}}(\alpha)$, or its constituents $I(\alpha)$ and $Q(\alpha)$. The U component vanishes due to the symmetric scattering geometry with respect to the principle plane. We use again the normalized Stokes parameter $p_Q(\alpha) = Q(\alpha)/I(\alpha)$ for the description of the polarization.

The Monte Carlo simulations were performed for $N_0 = 10^7$ incoming photons (flux F_0). The escaping photons are registered in the bins $\alpha_i = 2.5^\circ + i \cdot 5^\circ$, $i = 0 \dots 35$. The reflected intensities (relative to F_0) per solid angle from the illuminated star are obtained by the transformation $I_i = N_i/(\Omega_i N_0)$, where N_i are the counts registered in the bin α_i and $\Omega_i = \sin \alpha_i \cdot \pi^2/18$. Typical count rates are of the order 10^4 to 10^5 , giving statistical errors less than one per cent. In the following figures the $1\sigma_I$ error bars for the calculated intensity points are typically smaller than the size of the used symbols. But for phases around eclipse ($\alpha \approx 180^\circ$), where the photon source or the illuminated hemisphere is hidden by the star, none or only very few photons are registered. In this case the results are statistically less accurate, especially for the calculated polarization.

The ratio between the reflected Rayleigh scattered O VI photons and the total number of incoming photons define the spher-

ical albedo $A_{\text{Ray}} = \sum N_i/N_0$ for the illuminated star. The equivalent quantity for Raman scattered photons A_{Ram} can be used for characterizing the Raman conversion efficiency of the O VI emission lines in symbiotic systems.

5.2.1. Illumination by a parallel beam

We assume that a spherical body is illuminated by a parallel and unpolarized beam similar to the problem of planetary atmospheres. Calculated intensity $I(\alpha)$ and polarization $p_Q(\alpha)$ curves of the reflected Rayleigh and Raman scattered radiation are displayed in Figs. 7 and 8. Also given is in Fig. 7 by a dashed line the intensity curve for isotropic scattering ($a = 0.8$) computed from the analytical formulae of Chandrasekhar (1950) and integrated over the whole stellar disk.

The intensity curves have their maximum at $\alpha = 0^\circ$, when the photon source is in front of the illuminated star. The Rayleigh curve $I_{\text{Ray}}(\alpha)$ shows again the more pronounced peak for the backscattering direction ($\alpha = 0^\circ$). For $\kappa_{\text{red}} = 0$ and large phase angles $\alpha \gtrsim 90^\circ$ the Raman curve dominates, because grazing emergence is not suppressed. Maximum polarization is obtained around $\alpha = 90^\circ$ when scatterings occur mainly at right angles. For backscattering, $\alpha = 0^\circ$, no negative polarization is obtained in contrast to the plane parallel case. This comes from the fact that at conjunction the scattering geometry is symmetric with respect to the line of sight so that the polarizations from different parts of the illuminated atmosphere compensate. If the absorption cross sections κ_{uv} and κ_{red} are varied, the same behaviour for the intensity and polarization curves can be recognized as in the plane parallel case. For larger $\kappa_{\text{red}} = 0.4$ the Raman curve becomes a more pronounced maximum similar to the Rayleigh curve (Fig. 7). The polarization increases again with increasing absorption coefficients while the shape of the polarization curves remains almost unchanged. It can be seen that the polarization reacts more to changes of κ_{uv} .

Table 1. Reflection from a spherical star illuminated by a parallel beam. Mean (maximum) polarization P_{max} in the interval $85^\circ \leq \alpha \leq 95^\circ$ (given in per cent) of the Raman and Rayleigh scattered radiation for various absorption cross sections κ_{uv} and κ_{red} .

κ_{red}	κ_{uv}	0.00	0.05	0.10	0.20	0.40	1.00	5.00
Raman scattering								
0.00		49.5	54.2	58.0	63.9	72.0	83.1	95.1
0.05		52.9	57.1	60.6	66.0	73.4	83.8	95.2
0.10		54.8	58.8	62.1	67.2	74.2	84.2	95.2
0.20		57.7	61.3	64.3	69.0	75.5	84.8	95.3
0.40		61.4	64.6	67.2	71.3	77.1	85.6	95.4
1.00		67.3	70.0	72.0	75.2	80.1	87.2	95.6
5.00		76.7	78.8	79.9	82.1	85.7	90.4	96.2
Rayleigh scattering								
		67.3	70.3	72.7	76.6	81.4	88.4	96.3

$\sigma_{\text{Ray}} = 0.8$, $\sigma_{\text{Ram}} = 0.2$.

In Table 1 the maximum polarization around $\alpha = 90^\circ$ (mean polarization in the interval $85^\circ \leq \alpha \leq 95^\circ$) is given for different κ_{uv} and κ_{red} . The (absolute) statistical errors in this tabulation lie between ± 0.15 and ± 0.35 in P_{max} . The systematic underestimation of the true maximum polarization, due to averaging in an interval, amounts to approximately 0.2 (in P_{max}).

According to Table 1 absorption of O VI photons in the UV suppresses very efficiently multiple scatterings. For very large κ_{uv} most photons undergo only one scattering process and almost 100

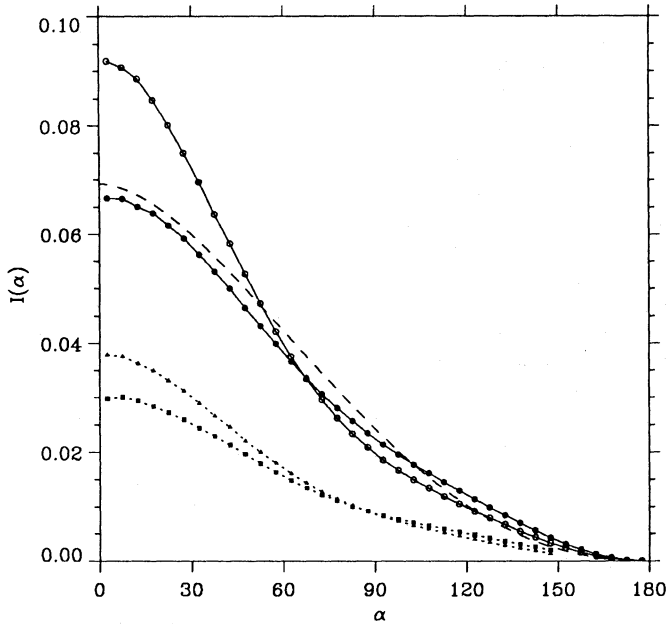


Fig. 7. Reflection from a spherical body illuminated by a parallel beam. Intensities I_{Ray} (open circles) and I_{Ram} (filled symbols) for zero absorption (circles), $\kappa_{\text{uv}} = 0.4$ (squares) and $\kappa_{\text{red}} = 0.4$ (triangles). The dashed line is the analytical solution for isotropic scattering ($a = 0.8$)

per cent polarization is achieved for a perpendicular scattering angle. Absorption of Raman scattered photons prevents only the escape from deeper layers where the less polarized (or more frequently scattered) radiation originates. Thus absorption in the red is less selective for those photons which undergo multiple scattering.

5.2.2. Illumination by point-like sources

We now assume that the O VI radiation is produced by a point-like source S . The position of this source is characterized by the ratio $q = D/R$ between the distance OS and the radius of the illuminated star. For finite distances the point source can not illuminate a full hemisphere of the reflecting star. The area exposed to the incident photons is defined by the tangent cone from point S to the spherical star (see Fig. 2). The boundary of this area is given by $\delta_{\text{max}} = 90^\circ - \varrho_{\text{max}} = 90^\circ - \arcsin(R/D)$. If the source is close to the star then a larger fraction of photons penetrate in the central region near point S' (small angles δ) into the atmosphere.

Compared to the case, where the star is illuminated by a parallel beam, the intensity and polarization light curves show some differences for small q values. (see Fig. 9 and 10). The intensity curves $I_{\text{Ram}}(\alpha)$ have a less pronounced maximum at $\alpha = 0$. No photons are registered for large angles $\alpha > 180^\circ - \varrho_{\text{max}}$ because at these phases the illuminated part of the atmosphere is completely hidden by the star itself. Further effects of point sources are that the maximum polarization P_{max} is lowered, and the angle where maximum polarization occurs α_{max} is shifted towards $\alpha < 90^\circ$.

The polarization around $\alpha = 90^\circ$ is mainly degraded because large parts of the star are illuminated by an inclined radiation field with respect to the principle plane. Therefore also the polarization direction of the reflected radiation is rotated by an angle which corresponds roughly to the inclination angle ϱ_\perp for

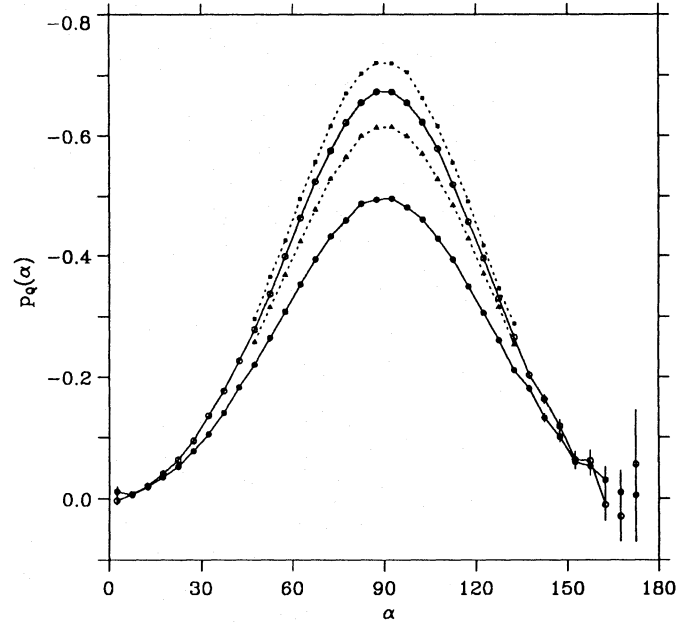


Fig. 8. The same as Fig. 7 for the normalized Stokes parameter $p_Q(\alpha) = Q/I$ with $1\sigma_p$ error bars. Points with $\sigma_p > 0.1$ are not given

the incoming radiation. Due to symmetric compensation of “upper and lower” hemisphere only the perpendicular polarization component remains, so that the net polarization is lowered.

Table 2. Reflection from a spherical star illuminated by a point source. Maximum percentage polarization P_{max} of the Raman and Rayleigh scattered radiation for various model parameters.

κ_{red}	κ_{uv}	$q = \infty$	10	5	3	2
Raman scattering						
0.0	0.0	49.6	48.8	47.7	45.0	40.2
0.0	0.2	64.0	63.8	62.5	58.7	52.6
0.0	1.0	83.2	82.4	80.9	76.5	67.4
0.2	0.0	57.7	57.1	56.0	52.8	46.8
1.0	0.0	67.3	66.8	65.6	61.5	54.0
Rayleigh scattering						
	0.0	67.3	66.9	65.3	61.6	53.9
	0.2	76.6	76.3	74.3	70.4	61.6
	1.0	88.5	87.9	86.1	81.3	71.5

$\sigma_{\text{Ray}} = 0.8$, $\sigma_{\text{Ram}} = 0.2$.

α_{max} is shifted because for a distant observer large fractions of the reflecting hemisphere are illuminated by a point source under a right angle before the quadrature (perpendicular) phase $\alpha = 90^\circ$ occurs. For close photon sources this behaviour is obviously more pronounced. Calculated angles α_{max} , where the polarization curves reach their maximum, are given in Table 3. The estimated errors for the α_{max} -values are approximately $0.2^\circ - 0.4^\circ$.

α_{max} depends, according to Table 3, also on the absorption cross section κ_{red} but not on κ_{uv} . This behaviour is in line with previous findings. As discussed in previous sections, enhancement of κ_{uv} changes for the escaping radiation not significantly the angle distribution of the intensity or the polarization. But enhancement of κ_{red} reduces the extreme limb brightening effect for the Raman scattered radiation (see Fig. 5). Therefore strong absorption κ_{red} lowers around $\alpha \approx 90^\circ$ the contribution of the

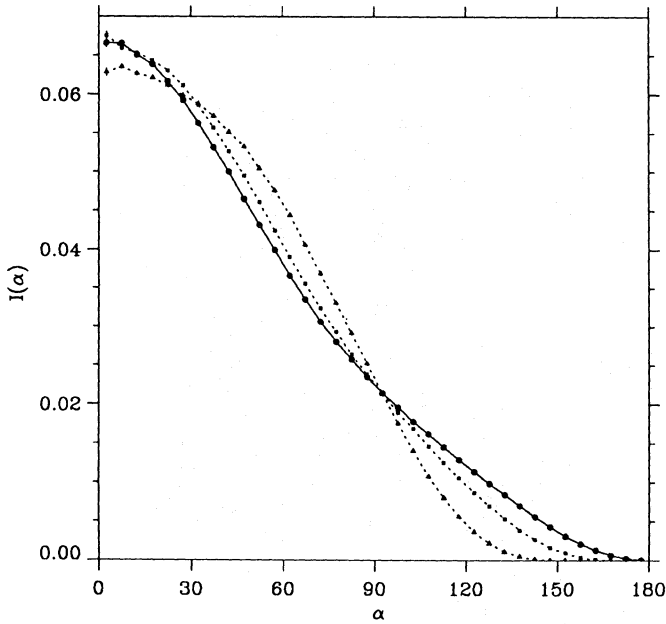


Fig. 9. Reflection from a spherical body illuminated by a point like source. Reflected intensities $I_{\text{Ram}}(\alpha)$ for a parallel photon beam (dots) and point sources with distances $q = 5$ (squares) and $q = 2$ (triangles)

bright limb facing the photon source, and thus changes the relative intensity distribution of the reflected light on the illuminated surface. For $\kappa_{\text{red}} \gg 0$ larger contributions come from regions well inside the limb so that perpendicular scatterings and therefore maximum polarization occurs for smaller escape direction angles α .

Table 3. Reflection from a spherical star illuminated by a point source. Angle of maximum polarization α_{max} for various model parameters.

κ_{red}	κ_{uv}	$q = \infty$	10	5	3	2
Raman scattering						
0.0	0.0	89.6°	87.9°	85.8°	83.5°	82.5°
0.0	0.2	89.7°	88.0°	85.7°	83.5°	82.2°
0.0	1.0	90.3°	87.6°	85.7°	83.8°	82.2°
0.2	0.0	90.1°	87.7°	85.1°	82.2°	80.2°
1.0	0.0	89.9°	87.1°	84.0°	80.5°	78.0°
Rayleigh scattering						
	0.0	90.0°	87.1°	84.2°	80.5°	77.5°
	0.2	89.9°	86.7°	83.9°	80.4°	77.3°
	1.0	89.9°	86.8°	84.0°	80.3°	77.3°

$\sigma_{\text{Ray}} = 0.8$, $\sigma_{\text{Ram}} = 0.2$.

5.2.3. Illumination by extended sources

Various models have been proposed for the geometric structure of the emission nebulae in symbiotic systems. We adopt here an extended source (corotating) which is shaped like a spherical cap with constant surface brightness. A similar structure for the emission nebula in symbiotic systems is obtained from elaborate model calculations where the hot component ionizes parts of the red giant wind (Nussbaumer & Vogel 1987; Schmid & Vogel, 1987). The cap is constructed by a rotationally symmetric superposition of point sources which is characterized by the distance D and the maximum angle ψ_{max} relative to the binary axis. For

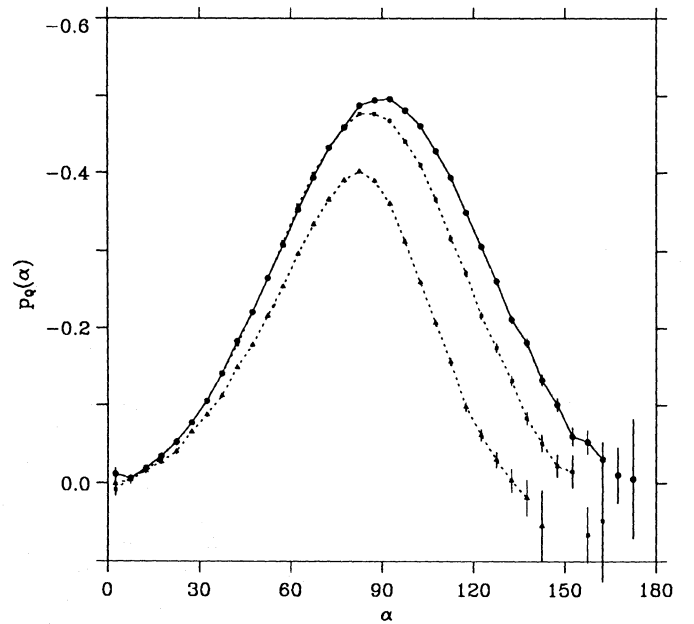


Fig. 10. The same as Fig. 9 for the normalized Stokes parameter $p_{\text{Ram}}(\alpha) = Q/I$ with $1\sigma_p$ error bars. Points with $\sigma_p > 0.1$ are not given

small ψ_{max} the photon source resembles a disk-like nebula with constant surface brightness.

For extended sources the intensity curves $I_{\text{Ray}}(\alpha)$ become somewhat flatter. For large ψ_{max} more than a hemisphere is illuminated so that even for phase angle $\alpha = 180^\circ$ (eclipse) some photons can be observed (Fig. 11).

Very characteristic are the polarization curves $p_Q(\alpha)$ plotted in Fig. 12. Much smaller polarizations are obtained. For extended sources the incoming photons have less uniform directions so that compensation becomes more and more important. This reduction of the polarization due to source extension is a well known effect in scattering problems (see Brown et al. 1989). The polarization maximum P_{max} is shifted towards larger angles $\alpha > 90^\circ$ in contrast to the situation for point-like sources. This is again a geometric effect. Maximum polarization is expected when the visible part of the reflecting atmosphere is mainly illuminated under a right angle. This condition is best fulfilled for extended sources if around quadrature $\alpha \gtrsim 90^\circ$ some parts of the reflecting hemisphere are eclipsed. Then the remaining visible part is illuminated by a smaller, but geometrically more compact fraction of the nebula, so that the directions of the incoming photons are more uniform.

5.3. Efficiency for Raman scattering

The reflected Rayleigh scattered O VI radiation from the whole illuminated star into all directions is called the spherical albedo A_{Ray} . A_{Ram} is defined as the corresponding quantity for the reflected Raman scattered radiation for the O VI lines. A_{Ray} and A_{Ram} are expressed in Table 4 in per cent of the incoming O VI photon flux. The statistical errors in Table 4 are smaller than 2 units in the last digit.

The intensity of the reflected radiation depends not only on the absorption and scattering cross sections, but also on the angle of incidence ϑ_0 as defined for the plane parallel atmosphere model. Photons with perpendicular direction of incidence tend to

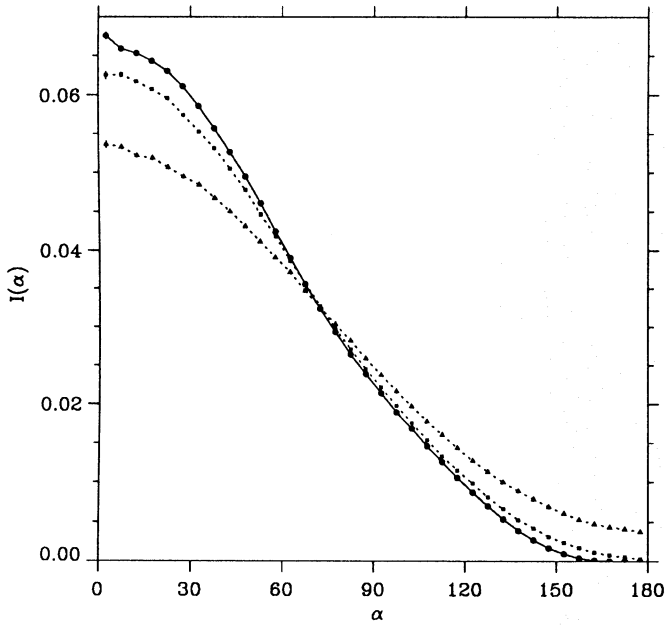


Fig. 11. Reflection from a spherical body illuminated by an extended source. Intensity curves $I(\alpha)$ are plotted for sources with $q = 5$ and extension $\psi_{\max} = 0^\circ$ or for a point source (points), $\psi_{\max} = 30^\circ$ (squares) and $\psi_{\max} = 60^\circ$ (triangles)

penetrate deeper into the atmosphere and are therefore relatively more frequently absorbed or converted into Raman photons. But the probability distribution function for the angles of incidence $\mathcal{P}(\theta_0)$ depends for an illuminated spherical star only little on the distance q of the photon source. Therefore the values A_{Ram} and A_{Ray} given in Table 4 are representative for all photon sources considered. For example the conversion efficiencies $A_{\text{Ram}}(\kappa_{\text{uv}}, \kappa_{\text{red}})$ for $q = 3$ differ less than 0.1 from the values given in Table 4. It is recalled that one half of the photons converted in a Raman scattering process have direction into the star and are absorbed. Thus at least (in the case $\kappa_{\text{red}} = 0$) as much Raman photons are destroyed as can escape. This explains why in Table 4 the sum of all reflected photons (Rayleigh and Raman scattered) is lower than 100 per cent even for zero absorption cross sections. It can be seen that the relative number of escaping Raman photons A_{Ram} decreases rapidly for increasing absorption.

Table 4. Conversion efficiency A_{Ram} and spherical albedo A_{Ray} (given in per cent) for Raman and Rayleigh scattered O VI lines. Results for a spherical body which is illuminated by a parallel beam.

κ_{red}	κ_{uv}	0.00	0.05	0.10	0.20	0.40	1.00	5.00
Raman scattering								
0.00		32.83	27.68	24.02	19.10	13.64	7.42	1.86
0.05		26.88	23.10	20.35	16.52	12.13	6.86	1.81
0.10		23.63	20.52	18.23	14.99	11.20	6.49	1.77
0.20		19.40	17.10	15.38	12.88	9.86	5.92	1.71
0.40		14.59	13.10	11.97	10.26	8.11	5.14	1.61
1.00		8.60	7.93	7.41	6.58	5.48	3.79	1.40
5.00		2.39	2.29	2.20	2.05	1.85	1.51	0.82
Rayleigh scattering								
		34.39	30.76	27.90	23.60	18.16	10.86	3.00

$\sigma_{\text{Ray}} = 0.8$, $\sigma_{\text{Ram}} = 0.2$.

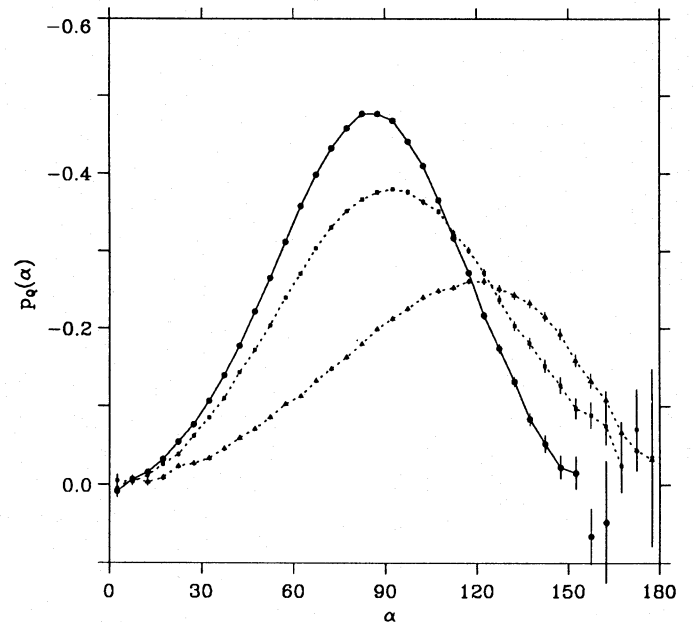


Fig. 12. The same as Fig. 11 for the normalized Stokes parameter $p_{\text{Ram}}(\alpha) = Q/I$ with $1\sigma_p$ error bars

The fraction of photons from the source illuminating the star changes strongly with the parameter $q = R/D$. In order to obtain the absolute efficiency, the values given in Table 4 must be scaled with f_ℓ as given in Eq. (15). Typical values for this geometric scaling factor are $f_\ell = 0.067, 0.029, 0.010$ and 0.0025 for $q = 2, 3, 5$ and 10 respectively. Thus in symbiotic stars only a few per cent of the O VI photons generated can be converted into Raman scattered photons. This rather low efficiency is further lowered quite rapidly for more distant photon sources or larger absorption cross sections.

The efficiencies for Rayleigh scattering A_{Ray} and Raman scattering A_{Ram} are roughly equal for vanishing κ_{red} . But it is mentioned again, that the Rayleigh scattered photons reflected from the illuminated star contribute only a few per cent or even less of the totally released O VI photons. Therefore the high polarization for Rayleigh scattered radiation as given in Tabs. 1 and 2 is in reality not observable. This polarization is almost lost in the unpolarized radiation field coming directly from the photon source. Contrary to this, only scattered light contributes to the Raman lines and their large polarization is preserved.

6. Differences between the $\lambda 6825$ and the $\lambda 7082$ components

In the previous chapter we discussed the general behaviour of the Raman scattered O VI lines. Now we concentrate on differences between the two components $\lambda 6825$ ($\lambda 1032$) and $\lambda 7082$ ($\lambda 1037$). From the observational point of view such differences are of interest because relative quantities may be measured more easily even when they are rather subtle. In Chap. 2 we discussed observed intensity ratios and differences in the polarization between the two Raman scattered lines.

According to Eq. (4) the ratios between the Rayleigh and Raman cross sections, $\sigma_{\text{Ray}}/\sigma_{\text{Ram}}$, are 5.2 and 3.0 for the $\lambda 1032$ and the $\lambda 1038$ line respectively. In the previous chapter a mean value of 4 was used. The individual cross sections will cause slight

Table 5. Monte Carlo simulation of Raman and Rayleigh scattered O VI lines reflected from a star, which is illuminated by a parallel beam. Conversion efficiency A_{Ram} and spherical albedo A_{Ray} , maximum polarization P_{max} and corresponding ratios Λ_A and Λ_P between the two components $\lambda 6825$ and $\lambda 7082$.

κ_{uv} in σ_e	κ_{red}	$\lambda 6825$ A_{Ram}	$\lambda 6825$ P_{max}	$\lambda 7082$ A_{Ram}	$\lambda 7082$ P_{max}	$2 \cdot \Lambda_A$	Λ_P
0	0	30.72	44.1	34.25	53.4	1.79	0.83
0	1	27.06	46.4	24.24	58.7	2.23	0.79
0	10	16.16	54.4	8.56	70.5	3.78	0.77
0	100	3.76	64.0	1.25	81.5	6.02	0.79
1	0	27.71	47.2	24.95	61.8	2.22	0.76
1	1	24.60	49.3	18.68	65.8	2.63	0.75
1	10	15.07	56.7	7.38	74.9	4.08	0.76
1	100	3.63	71.8	1.16	84.1	6.26	0.85
10	0	15.12	63.4	7.55	85.1	4.01	0.75
10	1	13.93	64.6	6.57	86.0	4.24	0.75
10	10	9.69	69.6	3.80	88.5	5.10	0.79
10	100	2.92	79.1	0.87	92.7	6.71	0.85
100	0	2.91	90.8	0.98	97.4	6.06	0.93
100	1	2.84	90.9	0.93	97.5	6.11	0.93
100	10	2.48	91.5	0.80	97.6	6.20	0.94
100	100	1.34	93.4	0.41	98.0	6.54	0.95

κ_{uv} in σ_e	$\lambda 1032$ A_{Ray}	$\lambda 1032$ P_{max}	$\lambda 1038$ A_{Ray}	$\lambda 1038$ P_{max}	$2 \cdot \Lambda_A$	Λ_P
0	38.58	64.0	31.49	69.5	2.45	0.92
1	36.23	65.9	25.19	75.1	2.88	0.88
10	23.94	76.3	9.43	89.8	5.08	0.85
100	5.84	93.4	1.33	98.1	8.78	0.95

σ_{Ray} and σ_{Ram} according to Eq. (4).

differences in the properties of the two lines with respect to each other. However the general behaviour of both Raman scattered lines does not differ qualitatively from the description given in Chap. 5.

For the longer wavelength component $\lambda 1038$ the scattering cross sections σ_{Ray} and σ_{Ram} are smaller by a factor of 5.1 and 3.3 respectively compared to $\lambda 1032$. Thus it is likely that absorbing particles will influence differently the intensity and polarization light curves of the two emission lines $\lambda 6825$ and $\lambda 7082$.

We restrict our discussion to models where a star is illuminated by a parallel beam.

6.1. Conversion efficiency and maximum polarization

In Table 5 the conversion efficiencies A_{Ram} and the maximum polarization P_{max} around phase $\alpha = 90^\circ$ of the Raman scattered emission lines $\lambda 6825$ and $\lambda 7082$ are given. Also listed are the ratios $2 \cdot \Lambda_A = 2 \cdot A_{\text{Ram}}(\lambda 6825)/A_{\text{Ram}}(\lambda 7082)$ and $\Lambda_P = P_{\text{max}}(\lambda 6825)/P_{\text{max}}(\lambda 7082)$. The ratio Λ_A has been multiplied by the factor 2 to account for the expected flux ratio for the O VI resonance doublet $I(\lambda 1032)/I(\lambda 1038) = 2$. Thus $2 \cdot \Lambda_A$ corresponds to a calculated “mean” ratio for the Raman scattered emission lines which can be compared with measurements of symbiotic stars.

For zero absorption the conversion efficiency $A_{\text{Ram}}(\lambda 7082)$ is larger than $A_{\text{Ram}}(\lambda 6825)$. This is caused by the lower cross section ratio $\sigma_{\text{Ray}}/\sigma_{\text{Ram}}$ for the longer wavelength component. Therefore O VI $\lambda 1038$ photons are converted on the average after less Rayleigh scatterings than the $\lambda 1032$ photons and thus rel-

atively more Raman photons $\lambda 7082$ are produced. Because less Rayleigh scattering (or multiple scatterings) occur for the $\lambda 1038$ ($\lambda 7082$) photons, the polarization is higher for this component, as discussed earlier.

Absorbing particles suppress the reflected radiation and enhance the polarization of the longer wavelength component much more efficiently. $2 \cdot \Lambda_A$ -ratios comparable with measured line ratios $I(\lambda 6825)/I(\lambda 7082) \approx 2 - 8$ are obtained for all absorption cross sections considered. For intermediate absorption cross sections $\approx 1 - 10\sigma_e$ the largest differences in the polarization between the two Raman lines (lowest Λ_P -values) are reached.

Up to now we have assumed that the absorption cross section κ_{red} for the two Raman scattered lines are equal. As outlined in Chap. 2 this simplification may not be valid for M-type atmospheres, because the longer wavelength component at $\lambda 7082$ coincides with the strong TiO-band at $\lambda 7054$. If $\kappa_{\text{red}}(\lambda 6825) \ll \kappa_{\text{red}}(\lambda 7082)$, the reflected intensity of the weaker component at $\lambda 7082$ is even more suppressed and the polarization more enhanced relative to the stronger component. As example one obtains with the results given in Table 5 for the cross sections $\kappa_{\text{red}}(\lambda 6825) = \sigma_e$, $\kappa_{\text{red}}(\lambda 7082) = 10 \cdot \sigma_e$, $\kappa_{\text{uv}} = \sigma_e$ the relative “line” and polarization ratios $2 \cdot \Lambda_A = 6.7$ and $\Lambda_P = 0.66$. Thus, rather extreme line and polarization ratios are obtained when $\kappa_{\text{red}}(\lambda 6825) \ll \kappa_{\text{red}}(\lambda 7082)$.

6.2. Changes depending on the angle α

The intensity and polarization of the Raman scattered lines change strongly with angle α . Therefore also variations in the line ratio of the two Raman scattered lines can be expected. The polarization ratios $\Lambda_P(\alpha)$ is more or less constant because the shapes of the polarization curves $p_Q(\alpha)$ depend not significantly on the scattering and absorption cross sections.

In Fig. 13 intensity ratios $2 \cdot \Lambda_I(\alpha) = 2 \cdot I_{\lambda 6825}(\alpha)/I_{\lambda 7082}(\alpha)$ are plotted as function of α for some absorption coefficients. A different behaviour is obtained for $\Lambda_I(\alpha)$ curves where $\kappa_{\text{red}}(\lambda 6825) = \kappa_{\text{red}}(\lambda 7082)$ and for curves with $\kappa_{\text{red}}(\lambda 6825) \ll \kappa_{\text{red}}(\lambda 7082)$. In the first case the $2 \cdot \Lambda_I(\alpha)$ curves depend little on α , so that the conversion efficiency ratios $2 \cdot \Lambda_A$, as given in Table 5, describe rather well the line ratio for all phase angles α . That absorption in the UV produces no large angle dependence of $\Lambda_I(\alpha)$ is in line with previous findings. It was found that the shape of the intensity curves $I(\alpha)$ are not significantly altered by different κ_{uv} values. It is, however, expected that absorption in the red produces angle dependent line ratios $\Lambda_I(\alpha)$, especially for grazing emergence. But according to Fig. 13 this effect is too small in the case $\kappa_{\text{red}}(\lambda 6825) = \kappa_{\text{red}}(\lambda 7082)$ to produce a strong deviation of the ratio $\Lambda_I(\alpha)$ from a constant value.

A clear gradient in the line ratio $\Lambda_I(\alpha)$ is obtained for the case $\kappa_{\text{red}}(\lambda 6825) \ll \kappa_{\text{red}}(\lambda 7082)$ when the absorption in the red is strongly selective as expected by absorbing TiO molecules. Then a pronounced angle dependence of the intensity ratio $\Lambda_I(\alpha)$ is coupled with strong and selective attenuation of the longer wavelength component $\lambda 7082$.

7. Interpretation of polarization variations

The results from the Monte Carlo simulations, given in Chap. 5, will now be used as diagnostic tool for deriving the inclination and the orientation of the orbital plane and other parameters

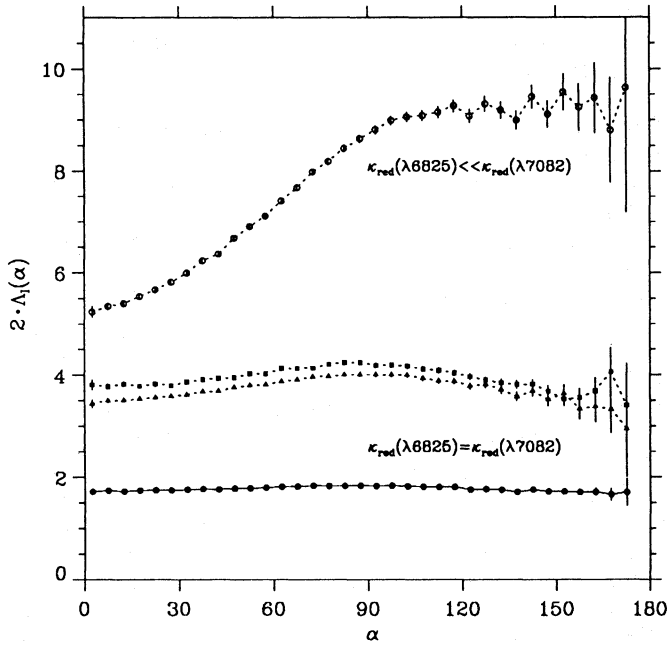


Fig. 13. Intensity ratio $2 \cdot A_I = 2 \cdot I_{\lambda 6825} / I_{\lambda 7082}$ as function of the angle α for zero absorption (points), $\kappa_{UV} = 10\sigma_e$ (squares), $\kappa_{red} = 10\sigma_e$ (triangles) and $\kappa_{red}(\lambda 6825) = 0, \kappa_{red}(\lambda 7082) = 10\sigma_e$ (circles)

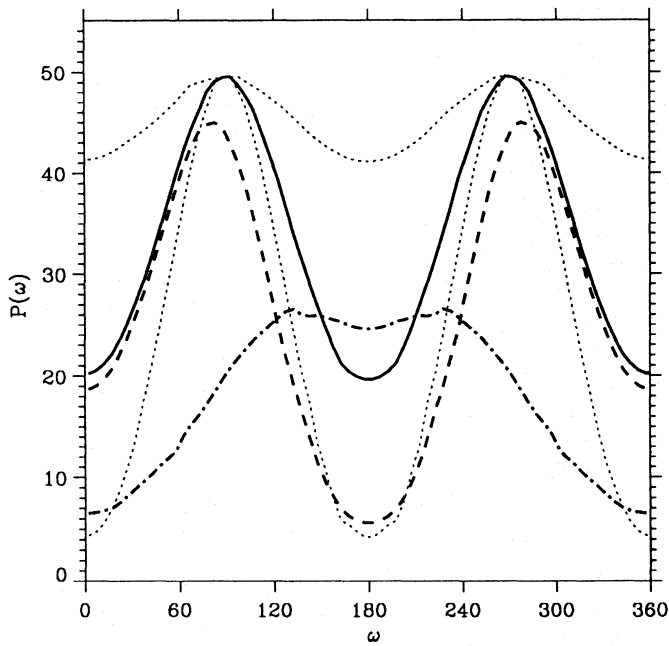


Fig. 14. Linear polarization P versus orbital phase angle ω for the reflected Raman scattered radiation. Systems with orbital inclination $i = 45^\circ$ (thick curves) and a parallel incoming photon beam (solid curve), a point source with $q = 3$ (dashed line) and an extended source with $q = 3, \psi_{max} = 60^\circ$ (dashed dotted line). Also given are the curves for systems with a parallel incoming photon beam and inclinations $i = 20^\circ$ and $i = 70^\circ$ (thin dotted lines)

of the system. In this chapter we use again the scattering cross section $\sigma_{Ray} = 0.8$, $\sigma_{Ram} = 0.2$ and neglect absorption.

The polarization of the Raman scattered emission lines in symbiotic stars is expected to change periodically due to the binary motion. Therefore we construct sequences for the relative polarization P and for the normalized Stokes parameters p_Q, p_U as function of the orbital angle ω and for different inclinations i . Similar geometric figures of theoretical and observational data were presented and analysed by Brown et al. (1978), Simmons (1983), Dolan (1984), St.-Louis et al. (1987) and others.

In Fig. 14 $P(\omega)$ curves are plotted for various model parameters. It can be seen that a large orbital inclination produces large variations in the relative polarization $P(\omega)$ while for small i the curve $P(\omega)$ is almost constant. It may be possible that information on the geometry of the photon source can be inferred from the shape of the $P(\omega)$ curves. Regular double waves result from models where the star is illuminated by a parallel photon beam. For point like sources the polarization minimum at $\omega = 0^\circ$ is larger than the minimum at $\omega = 180^\circ$ and the phase for maximum polarization ω_{max} is shifted towards phase $\omega = 0^\circ$ (360°). The contrary $P(0^\circ) < P(180^\circ)$ and a shift of ω_{max} towards $\omega = 180^\circ$ happens for extended sources. Other parameters, which have not been considered in this work, may however modulate the shape of the $P(\omega)$ curves as well.

Fortunately the ratio $R_P = P(0^\circ)/P(90^\circ)$ between the relative polarizations at conjunction ($\omega = 0^\circ$) and at quadrature is a step function of the orbital inclination and depends only little on the geometric structure of the photon source. This is shown in Fig. 15, where the $R_P(i)$ curves for all models presented in the Figs. 7–12 are plotted. Thus the inclination of the orbital plane can be derived quite accurately from this simple graph. For a given inclination point sources tend to have larger and extended sources smaller R_P -values. But these deviations from the general behaviour must only be considered for the most extreme cases.

When analysing the $P(\omega)$ curves we neglect the information included in the polarization direction. But especially for determining the orientation of the ascending node Ω of the binary plane with respect to the celestial sphere we need this information. Therefore it is convenient to compare observational data also with sequences of p_Q and p_U values from the Monte Carlo simulations. $p_Q = Q/I$ and $p_U = U/I$ are the normalized polarization parameters with respect to a given observer's reference axis (north celestial pole).

In Figs. 16 and 17 calculated loci p_Q, p_U for the Raman scattered radiation reflected from an illuminated star are plotted. For all curves the orientation of the ascending node is north, or $\Omega = 0^\circ$, and the rotation of the binary is counterclockwise. The phase $\omega = 0^\circ$ is indicated by a heavy dot. For the sake of clearness the first branch from $\omega = 0^\circ$ to 180° has been plotted by a heavy solid line and the second branch by a thin line. The branches are symmetric to each other according to $p_U(\omega) = -p_U(360^\circ - \omega)$.

Figure 16 shows the change of the p_Q, p_U -curves with orbital inclination. For $i = 10^\circ$ almost a double-looped circular curve is obtained. Thus mainly the polarization direction changes while the amount of polarization is almost constant. For higher inclinations the curve becomes more elongated and converges to a straight line for $i \rightarrow 90^\circ$.

If the orientation of the ascending node Ω is changed then the double-looped curves are rotated in the same direction and by the same rotation angle. Thus mapping the measured p_Q, p_U -observations is likely to provide the orientation of the ascending node. For small inclination the determination is more difficult, because the p_Q, p_U -curves are almost circular. Additionally the changes produced by interstellar grains must be considered, which

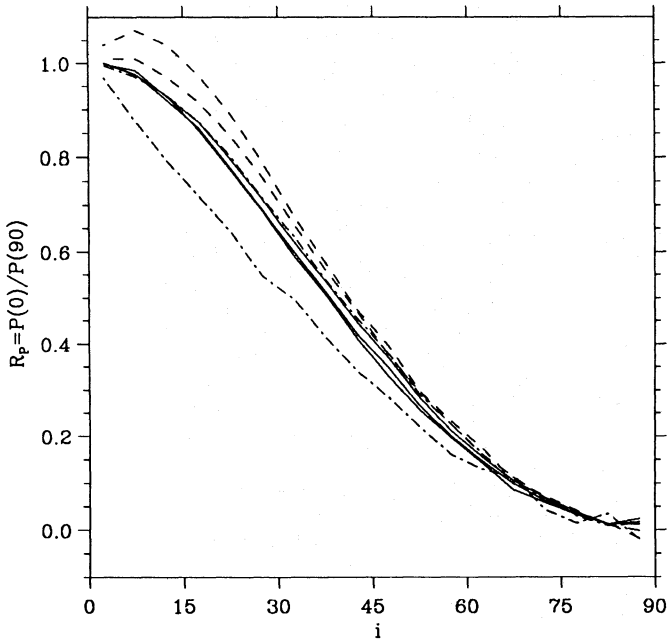


Fig. 15. Polarization ratios $R_P = P(0^\circ)/P(90^\circ)$ as function of the inclination for different models: parallel beam sources (solid lines), point sources (dashed lines) and extended sources (dashed dotted lines)

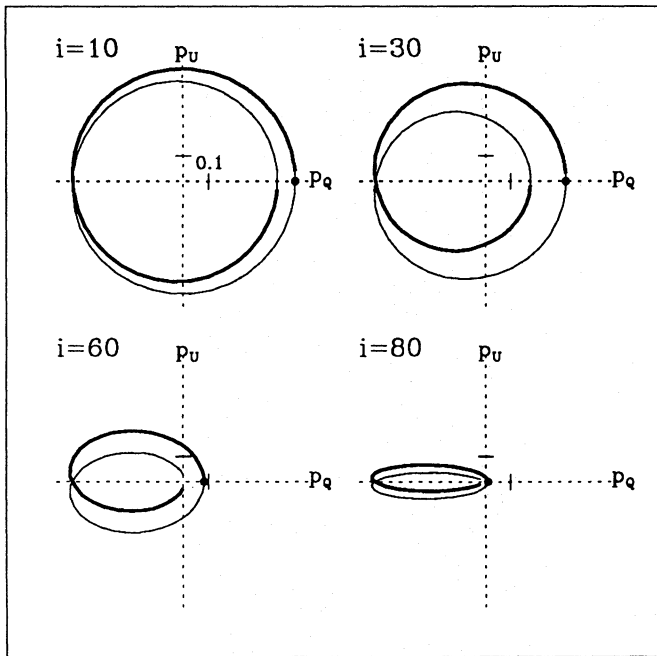


Fig. 16. Stokes parameter loci p_Q, p_U swept out during the binary period for Raman scattered radiation. Model parameters are: point source with $q = 3$ and zero absorption

may cause a displacement and a rotation of the p_Q, p_U -curves. However the shape of the double looped curves is not changed.

Figure 17 shows that the p_Q, p_U -curves depend also on the geometric properties of the photon source. The main difference between point-like and extended sources is that in the first case the heavy solid curve (first branch) spirals in and in the latter

case it spirals out. This is another manifestation of the different shapes of the polarization curves $P(\omega)$ where $P(0^\circ) > P(180^\circ)$ for point-like sources and $P(0^\circ) < P(180^\circ)$ for extended sources.

The relation between R_P and i (Fig. 15) or the flattening of the p_Q, p_U -curves with i (Fig. 16) are quite general for the scattering polarization coming from binary systems. The same behaviour has been found in previous studies cited above for a wide variety of situations. Thus the described basic polarization properties will not change strongly for somewhat different models.

8. Summary and conclusions

The properties of the Raman scattered O VI emission lines $\lambda\lambda 6825, 7082$ have been investigated with Monte Carlo simulations.

In the simulations the O VI $\lambda\lambda 1032, 1038$ line photons are released from a corotating photon source, which is located on or close to the binary axis (near the hot component), in order to mimic the O^{+5} nebular region of symbiotic systems. These photons penetrate into the atmosphere of the cool giant, where they are Rayleigh and Raman scattered or absorbed. We calculate the intensity and polarization of the reflected photons. Very high scattering polarizations are expected for $\lambda\lambda 6825, 7082$, because all photons in the Raman lines are produced in a scattering process. In contrast to coherent scattering problems (e.g. Rayleigh and Thomson scattering), the Raman scattered lines are not diluted by light coming directly from the source.

The results of the simulations are compared with the available observational data. They can easily reproduce with reasonable model parameters the observed line ratios $\Lambda_I = I_{\lambda 6825}/I_{\lambda 7082} \approx 2-8$ and the larger polarization seen for the weaker component at $\lambda 7082$. This suggests that our model, its geometric configuration and atomic processes, represents a reasonable approximation to the situation in real symbiotic systems.

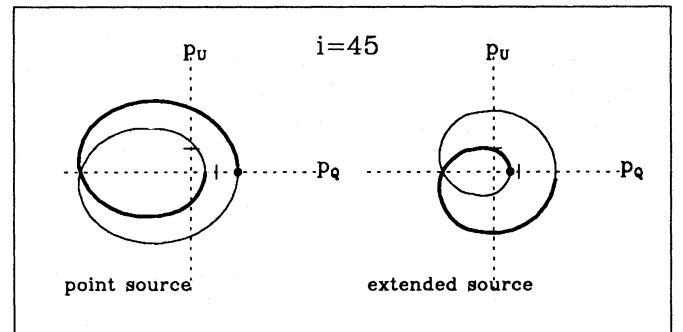


Fig. 17. The same as Fig. 16 for a point source ($q = 3$) and an extended source ($q = 3, \psi_{\max} = 60^\circ$)

Future observations and Monte Carlo simulations of the Raman scattered emission lines $\lambda\lambda 6825, 7082$ will offer various opportunities for deriving basic parameters of symbiotic systems: (i) The orbital parameters like period, inclination and the orientation of the line of node Ω with respect to the celestial sphere can be obtained from the polarization curve $P(\omega)$ or the corresponding figures in the p_Q, p_U -plane.

The period follows directly from the rotation of the polarization direction due to the rotation of the binary axis (or the scattering geometry) relative to the line of sight. This is particularly useful in cases where the orbital plane lies almost perpendicular to the line of sight and where therefore no radial velocity

variations or luminosity changes (e.g. due to the reflection effect) are measurable. Polarization direction changes are probably the only available tool to determine periods for symbiotic systems containing Miras, where very long orbital periods > 10 years are expected. Time coverage of about one fourth of the orbit already allows an estimate on the periods.

The inclination i is derivable from the ratios $R_p = P(0^\circ)/P(90^\circ)$ between the relative polarization at conjunction (light maximum) and quadrature. Knowledge of the inclination allows in combination with (existing) radial velocity measurements better estimates on stellar masses. Also the interpretation of the spectroscopic and photometric behaviour of symbiotic stars will be simplified if the orbital inclination is known.

The angle Ω which defines the orientation of the line of node with respect to the celestial coordinates follows from the double looped p_Q, p_U -curves. The polarization direction must however be corrected for the rotation produced by interstellar grains. Ω and i define the orientation of the orbital plane with respect to the celestial sphere. Knowledge of this information is of primary interest if bipolar structures and jet features of symbiotic systems are analysed.

(ii) Information on the geometry of the O^{+5} region in symbiotic systems can be derived from the polarization and intensity light curves. For point-like $O\text{ VI}$ line sources there is $P(0^\circ) > P(180^\circ)$ and for extended sources $P(0^\circ) < P(180^\circ)$ and the phase for maximum polarization around quadrature is shifted differently for point-like and extended sources. Further the systems with a point-like source tend to have more pronounced polarization and line flux variations.

(iii) Properties of the gas in the outer atmosphere of symbiotic giants can also be estimated. The intensity and polarization of Raman scattered emission lines depend strongly on the continuum absorption cross section in the ultraviolet κ_{uv} and in the red $\kappa_{red}(\lambda 6825)$, $\kappa_{red}(\lambda 7082)$. Future observations will also show if additional processes, like depolarizing collisions or isotropic scatterings must be considered. Informations on such quantities can be obtained for many different giants, with spectral types ranging from G to M8, Mira variables and carbon stars.

Additional diagnostic properties of the Raman scattered emission lines can be found in Schmid (1989) and Nussbaumer et al. (1989).

We like to recall here, that the present calculations were performed for simplified models. For example it was assumed that the illuminated star has a well defined surface although symbiotic Miras are known to possess extremely extended and tenuous outer atmospheres. An adequate treatment of such cases would require photon path simulations in a spherical geometry instead of a slab geometry. Other simplifications, such as neglecting additional atomic processes, have been made. This should be borne in mind, when observational data are analysed. However, the basic polarization properties are largely independent of complicating factors such as extended atmospheres.

In any case the emission lines $\lambda\lambda 6825, 7082$ form a powerful diagnostic tool for determining basic parameters in symbiotic

binaries. Because Raman lines have very favourable properties they may also provide a key for the understanding of scattering processes in stellar systems.

Acknowledgements. I am grateful to J.O. Stenflo for clarifying discussions. I wish to thank H. Nussbaumer, H. Schild and U. Mürset for assistance and numerous helpful comments. This work has been supported by a grant from the Swiss National Science Foundation.

References

- Abhyankar K.D., Fymat A.L., 1970, A&A 4, 101; erratum, A&A 5, 491
 Abhyankar K.D., Fymat A.L., 1971, ApJS 23, 35
 Allen D.A., 1979, in: Changing Trends in Variable Star Research, eds. Bateson et al., IAU Coll. 46, p.125
 Allen D.A., 1980, MNRAS 190, 87
 Bastien P., 1988, in: Polarized Radiation of Circumstellar Origin, eds. Coyne et al., Vatican Observatory, p.595
 Brown J.C., McLean I.S., Emslie A.G., 1978, A&A 68, 415
 Brown J.C., Carlaw V.A., Cassinelli, J.P., 1989, A&A 344, 341
 Cashwell E.D., Everett D.J., 1959, A practical manual on the Monte Carlo method for random walk problems, Pergamon Press, London
 Chandrasekhar S., 1950, Radiative Transfer, Clarendon Press, Oxford
 Cochran W.D., 1981, in: Planetary Aeonomy and Astronomy, Proc. of the 23. COSPAR meeting, eds. Atreya & Caldwell, Adv. Space. Res., Vol. 1, No. 9, p. 143
 Dolan J.F., 1984, A&A 138, 1
 Garcia M.R., Kenyon S.J., 1988, in: The Symbiotic Phenomenon, IAU Coll. 103, eds. Mikolajewska et al., Kluwer, p. 27
 Gonzalez-Riestra R., Cassatella A., Fernandez-Castro T., 1990, A&A 237, 385
 Isliker H., Nussbaumer H., Vogel M., 1989, A&A 219, 271
 Nussbaumer H., Vogel M., 1987, A&A 182, 51
 Nussbaumer H., Schmid H.M., Vogel M., 1989, A&A 211, L27
 Rudy R.J., Kemp J.C., 1978, ApJ 221, 200
 Schmid H.M., 1989, A&A 211, L31
 Schmid H.M., Schild H., 1990, A&A 236, L13
 Schmid H.M., Vogel M., 1987, ApSS 131, 707
 Simmons J.F.L., 1983, MNRAS 205, 153
 Stenflo J.O., 1976, A&A 46, 61
 St.-Louis N., Drissen L., Moffat A.F.J., Bastien P., 1987, ApJ 322, 870
 van de Hulst H.C., 1980, Multiple Light Scattering, 2 Volumes, Academic Press, New York
 Vogel M., 1991, A&A (in press)

This article was processed by the author using Springer-Verlag T_EX A&A macro package 1991.